

SMASH – SURVEY OF THE MAGELLANIC STELLAR HISTORY

DAVID L. NIDEVER^{1,2,3,4}, KNUT OLSEN¹, ALISTAIR R. WALKER⁵, A. KATHERINA VIVAS⁵, ROBERT D. BLUM¹, CATHERINE KALEIDA⁶, YUMI CHOI³, BLAIR C. CONN^{7,8}, ROBERT A. GRUENDL^{9,10}, ERIC F. BELL⁴, GURTINA BESLA³, RICARDO R. MUÑOZ^{11,12}, CARMEL GALLART^{13,14}, NICOLAS F. MARTIN^{15,16}, EDWARD W. OLSZEWSKI³, ABHIJIT SAHA¹, ANTONELA MONACHESI¹⁷, MATTEO MONELLI^{13,14}, THOMAS J. L. DE BOER¹⁸, L. CLIFTON JOHNSON¹⁹, DENNIS ZARITSKY³, GUY S. STRINGFELLOW²⁰, ROELAND P. VAN DER MAREL⁶, MARIA-ROSA L. CIONI^{21,22,23}, SHOKO JIN²⁴, STEVEN R. MAJEWSKI²⁵, DAVID MARTINEZ-DELGADO²⁶, LARA MONTEAGUDO^{13,14}, NOELIA E. D. NOËL²⁷, EDOUARDO J. BERNARD²⁸, ANDREA KUNDER²², YOU-HUA CHU^{29,10}, CAMERON P. M. BELL²², FELIPE SANTANA¹¹, JOSHUA FRECHEM³⁰, GUSTAVO E. MEDINA¹¹, VAISHALI PARKASH³¹, JACQUELINE SÉRON⁵, CHRISTIAN HAYES²⁵

Draft version January 4, 2017

ABSTRACT

The Large and Small Magellanic Clouds (LMC and SMC) are unique local laboratories for studying the formation and evolution of small galaxies in exquisite detail. The Survey of the MAGellanic Stellar History (SMASH) is an NOAO community DECam survey of the Clouds mapping 480 deg² (distributed over ~2400 deg² at ~20% filling factor) to ~24th mag in *ugriz* with the goal of identifying broadly distributed, low surface brightness stellar populations associated with the stellar halos and tidal debris of the Magellanic Clouds. SMASH will also derive spatially-resolved star formation histories covering all ages out to large radii from the MCs that will further complement our understanding of their formation. Here, we present a summary of the survey, its data reduction, and a description of the first public Data Release (DR1). The SMASH DECam data have been reduced with a combination of the NOAO Community Pipeline, PHOTRED, an automated PSF photometry pipeline based mainly on the DAOPHOT suite, and custom calibration software. The attained astrometric precision is ~15 mas and the accuracy is ~2 mas with respect to the Gaia DR1 astrometric reference frame. The photometric precision is ~0.5–0.7% in *griz* and ~1% in *u* with a calibration accuracy of ~1.3% in all bands. The median 5 σ point source depths in *ugriz* bands are 23.9, 24.8, 24.5, 24.2, 23.5 mag. The SMASH data already have been used to discover the Hydra II Milky Way satellite, the SMASH 1 old globular cluster likely associated with the LMC, and very extended stellar populations around the LMC out to projected $R \sim 22^\circ$ (18.4 kpc). The first public data release (“SMASH DR1”) contains measurements of ~100 million objects distributed in 61 discrete fields. A prototype version of the NOAO Data Lab provides access and exploration tools for the data release, including a custom Data Discovery tool, database access to the SMASH catalog, an image cutout service, and a Jupyter notebook server with example notebooks for exploratory analysis.

Subject headings: dwarf galaxy: individual: Large Magellanic Cloud, Small Magellanic Cloud — Local Group — Magellanic Clouds — surveys

1. INTRODUCTION

¹ National Optical Astronomy Observatory, 950 North Cherry Ave, Tucson, AZ 85719 (dnidever@noao.edu)

² Large Synoptic Survey Telescope, 950 North Cherry Ave, Tucson, AZ 85719

³ Steward Observatory, University of Arizona, 933 North Cherry Avenue, Tucson AZ, 85721

⁴ Department of Astronomy, University of Michigan, 1085 S. University Ave., Ann Arbor, MI 48109-1107, USA

⁵ Cerro Tololo Inter-American Observatory, National Optical Astronomy Observatory, Casilla 603, La Serena, Chile

⁶ Space Telescope Science Institute, 3700 San Martin Drive, Baltimore, MD 21218

⁷ Research School of Astronomy & Astrophysics, Mount Stromlo Observatory, Cotter Road, Weston Creek, ACT 2611, Australia

⁸ Gemini Observatory, Recinto AURA, Colina El Pino s/n, La Serena, Chile.

⁹ National Center for Supercomputing Applications, 1205 West Clark St., Urbana, IL 61801, USA

¹⁰ Department of Astronomy, University of Illinois, 1002 West Green St., Urbana, IL 61801, USA

¹¹ Departamento de Astronomía, Universidad de Chile, Camino del Observatorio 1515, Las Condes, Santiago, Chile

¹² Visiting astronomer, Cerro Tololo Inter-American Observatory, National Optical Astronomy Observatory, which is operated by the Association of Universities for Research in Astronomy (AURA) under a cooperative agreement with the National Science Foundation.

-eps-converted-to.pdf

The Large and Small Magellanic Clouds (LMC and SMC), as two of the nearest and most massive satellite galaxies of the Milky Way (MW), offer a unique opportunity to study the processes of galaxy formation and evolution of low-mass galaxies in great detail. The Clouds have long held broad importance for astronomy, with nearly 5000 papers referring to them by keyword. As the closest example of an interacting pair of galaxies, they provide special insight into the impact of such interactions on the structure and evolution of galaxies.

The Clouds are ideally suited to addressing some particularly critical questions: What are the consequences of stripping of stars and gas when dwarf galaxies fall into the halos of more massive galaxies, an important mode of mass growth for galaxies since $z \sim 1$? What are the properties of the hot and warm gaseous halos of galaxies like the Milky Way, the density of which sets the efficiency of gas stripping and “quenching” of satellites? What are the physical mechanisms and timescales, if any, behind the triggering of star formation by galaxy interactions?

de Vaucouleurs (1955) began the systematic study of the Magellanic Clouds (MCs), highlighting the young

and bright structures that trace the LMC's bar and the SMC's very irregular shape. Although the gaseous component of the LMC's disk extends only to a radius of $\sim 4^\circ$ (Staveley-Smith et al. 2003), the stellar component stretches over a much larger area. Stellar catalogs from the large near-infrared surveys DENIS (Epchtein et al. 1997) and 2MASS (Skrutskie et al. 2006) show it extending to at least $\sim 8^\circ$ and were used to measure the LMC disk structure and viewing angle (van der Marel 2001; van der Marel & Cioni 2001). Furthermore, carbon stars from Kunkel et al. (1997) follow disk kinematics out to $\sim 13^\circ$ (van der Marel et al. 2002). Finally, the Outer Limits Survey (OLS; Saha et al. 2010) used deep photometry to study old LMC main-sequence stars and found that in the north it followed the disk exponential profile out to $\sim 16^\circ$.

Evidence has been mounting for a halo component and substructures in the periphery of the LMC. Minniti et al. (2003) found kinematical evidence for an old LMC stellar halo using RR Lyrae stars (in the central region) with a large velocity dispersion. In the LMC outskirts, Muñoz et al. (2006) discovered a kinematically cold group of LMC stars in the foreground of the Carina dwarf spheroidal galaxy. Subsequently, the Magellanic Periphery Survey (MAPS; described in Nidever et al. 2011) used spectroscopically-confirmed red giant branch stars to detect a halo-like stellar population extending out to $\sim 22^\circ$ (over an $\sim 180^\circ$ azimuthal range) following a shallow de Vaucouleurs profile (Majewski et al. 2009). More recently, Mackey et al. (2016) used the Dark Energy Survey (DES; Dark Energy Survey Collaboration et al. 2016) data to detect an “arc-like” structure

in the periphery of the LMC (at $\sim 15^\circ$ from the center) which is likely a tidally disturbed portion of the LMC disk due to the recent interaction with the SMC. In addition, Belokurov et al. (2016) used the DES data to map streams of Blue Horizontal Branch (BHB) stars around the MCs with some extending to $R \sim 40^\circ$.

In the SMC, early photometric plate photometry showed that the young blue stars (produced by recent intense star formation) have a very irregular and patchy distribution while the older population (traced by giant stars) is fairly azimuthally symmetric and extends to larger radii ($\sim 5^\circ$; Hatzidimitriou & Hawkins 1989; Gardiner & Hawkins 1991; Gardiner & Hatzidimitriou 1992), as expected for dIrr galaxies (Mateo 1998). Subsequent deep CCD photometry by Noël & Gallart (2007) found old stellar populations out 5.8° and De Propriis et al. (2010) detected red giant stars spectroscopically out to $\sim 6^\circ$. The MAPS survey used photometrically selected red giant stars to find that the older SMC stellar population followed the same exponential profile from the center of the SMC out to $\sim 7.5^\circ$ but that beyond that there was a break in the radial profile with stars extending out to $\sim 11^\circ$ potentially representing a classical stellar halo of the SMC. In addition, Nidever et al. (2013) found evidence for a stellar component of the tidally stripped Magellanic Bridge and, more recently, Belokurov & Koposov (2016) used Gaia DR1 data to find both young and old stellar bridges, though not spatially coincident, between the Clouds. Finally, Pieres et al. (2016) used DES data to discover a stellar overdensity in the northern region of the SMC (at $\sim 8^\circ$) that might be a tidally stripped dwarf galaxy.

The complex interaction history of the Magellanic Clouds (with each other and the MW) that has produced the gaseous Magellanic Stream, Leading Arm and Bridge (Putman et al. 2003; Stanimirović et al. 1999; Muller et al. 2003; Brüns et al. 2005; Nidever et al. 2008, 2010), has been explored for over three decades (e.g., Murai & Fujimoto 1980; Gardiner & Noguchi 1996; Yoshizawa & Noguchi 2003; Connors, Kawata, & Gibson 2004, 2006; Mastropietro et al. 2005; Besla et al. 2012; Besla et al. 2013). Many of the features of the Magellanic system were well reproduced by a model invoking tidal stripping through repeated close passages to the MW by the MCs on their bound orbit (e.g., Gardiner & Noguchi 1996), although ram pressure stripping (e.g., Mastropietro et al. 2005) and star formation feedback (e.g., Olano 2004; Nidever et al. 2008) were also put forward as origin mechanisms and are likely important factors. However, in the last decade, some significant discoveries have been made about the MCs that raise fresh questions about their structure and past evolution. Perhaps most surprising is the discovery, based on HST proper motions of the MCs (Kallivayalil et al. 2006a; Kallivayalil et al. 2006b; Kallivayalil et al. 2013), that the MCs are likely approaching the MW environment for the first time (Besla et al. 2007). This discovery has forced a reinterpretation of many features of the Magellanic System, leading recent simulations (Besla et al. 2010, 2012; Diaz & Bekki 2012) to suggest that LMC-SMC interactions alone are responsible for the formation of the HI Magellanic Stream system that is now known to extend for at least 200° across the sky (Nidever et al. 2010).

The consequences of this new picture for the stellar

¹³ Instituto de Astrofísica de Canarias, La Laguna, Tenerife, Spain

¹⁴ Departamento de Astrofísica, Universidad de La Laguna, Tenerife, Spain

¹⁵ Université de Strasbourg, CNRS, Observatoire astronomique de Strasbourg, UMR 7550, F-67000 Strasbourg, France

¹⁶ Max-Planck-Institut für Astronomie, Königstuhl 17, D-69117 Heidelberg, Germany

¹⁷ Max-Planck-Institut für Astrophysik, Karl-Schwarzschild-Str. 1, 85748 Garching, Germany

¹⁸ Institute of Astronomy, University of Cambridge, Madingley Road, Cambridge CB3 0HA, UK

¹⁹ Center for Astrophysics and Space Sciences, UC San Diego, 9500 Gilman Drive, La Jolla, CA, 92093-0424, USA

²⁰ Center for Astrophysics and Space Astronomy, University of Colorado, 389 UCB, Boulder, CO, 80309-0389, USA

²¹ Universität Potsdam, Institut für Physik und Astronomie, Karl-Liebknecht-Str. 24/25, 14476 Potsdam, Germany

²² Leibniz-Institut für Astrophysik Potsdam (AIP), An der Sternwarte 16, 14482 Potsdam Germany

²³ University of Hertfordshire, Physics Astronomy and Mathematics, Hatfield AL10 9AB, United Kingdom

²⁴ STFC RALSpace, Rutherford Appleton Laboratory, Harwell Oxford OX11 0QX UK

²⁵ Department of Astronomy, University of Virginia, Charlottesville, VA 22904, USA

²⁶ Astronomisches Rechen-Institut, Zentrum für Astronomie der Universität Heidelberg, Mönchhofstr. 12-14, 69120 Heidelberg, Germany

²⁷ Department of Physics, University of Surrey, Guildford, GU2 7XH, UK

²⁸ Université Côte d'Azur, OCA, CNRS, Lagrange, France

²⁹ Institute of Astronomy and Astrophysics, Academia Sinica, No.1, Sec. 4, Roosevelt Rd, Taipei 10617, Taiwan, R.O.C.

³⁰ Rochester Institute of Technology, Rochester, NY 14623

³¹ Monash Centre for Astrophysics, School of Physics and Astronomy, Monash University, Victoria 3800, Australia

component of the MCs are only beginning to be explored. Nevertheless, we now know that MC stellar populations can be found over large areas of sky; that the LMC has stripped a large number of stars from the SMC ($\sim 5\%$ of the LMC’s mass, Olsen et al. 2011); and that strong population gradients exist to large radii (Gallart et al. 2008; Cioni 2009). In addition, the advent of the $\sim 5000 \text{ deg}^2$ DES has given rise to the discovery of many new satellite galaxies (Bechtol et al. 2015; Koposov et al. 2015; Drlica-Wagner et al. 2015), some of which are likely associated with the Magellanic Clouds (Deason et al. 2015; Jethwa et al. 2016; Walker et al. 2016; Sales et al. 2017). These results point to a much richer and more complex structure and history than was imagined just a few years ago.

Most previous surveys of the MCs were based on pencil-beam searches of only $\sim 1\%$ of the relevant area or were focused on the central MCs (e.g., MCPS; Zaritsky et al. 2002). With the advent of large imagers such as the Dark Energy Camera (DECam; Flaugher et al. 2015) on the NOAO Blanco 4-m telescope at Cerro Tololo Inter-American Observatory (CTIO), the door has been opened to pursue a more systematic and deep study of the Magellanic environs.

Our Survey of the MAgellanic Stellar History (SMASH) aims to measure the extended stellar populations of the Clouds and their detailed star formation histories in the central regions, which combined will allow us to develop general ideas regarding galaxy evolution in quantitative detail. SMASH is an NOAO survey project using DECam to map 480 deg^2 of the Magellanic periphery and main bodies (distributed over $\sim 2400 \text{ deg}^2$ at $\sim 20\%$ filling factor) with deep *ugriz* images. Our survey builds on the technique first adopted by the Outer Limits Survey; namely, we aim to use old main sequence stars as tracers to reveal the relics of the formation and past interactions of the Clouds down to surface brightnesses equivalent to $\Sigma_g = 35 \text{ mag arcsec}^{-2}$ over a vast area. The main project goals are:

- Search for the stellar component of the Magellanic Stream and Leading Arm. The detection of stellar debris in these structures would make them the only tidal streams with known gaseous and stellar components in the Local Group. This would not only be invaluable for understanding the history and observable consequences of the Magellanic interaction, but would give us a “clean” dynamical tracer of the MW’s dark halo and a way to prove the efficiency of the MW’s hot halo gas to induce ram pressure effects.
- Detect and map the smooth components of the Clouds, including their extended disks and stellar halos. The size of the LMC’s stellar periphery is a direct probe of the tidal radius of the LMC, with which we can explore the dark matter halos of the LMC and MW.
- Detect and map potential streams, satellites and substructure in the Magellanic periphery not associated with HI features. These would probe stages in the formation and interaction of the Clouds at times earlier than the HI dissipation timescale.

- Derive spatially resolved, precise star formation histories covering all ages of the MCs and to large radii, thus providing detailed information on their complete evolution.
- Enable many community-led projects, including studies involving the LMC/SMC main bodies, Galactic structure, discovery of variable objects, and background galaxy populations.

The aim of this paper is to describe the survey and provide details on the pipelines that produced the photometric catalogs and information regarding the first public data release. The layout of this paper is as follows. Sections 2 and 3 detail the survey and observing strategy. An overview of the data reduction is given in Section 4 while the calibration is discussed in Section 5. A description of the final catalogs and the achieved performance is given in Section 6. The details of the first SMASH data release and data access are described in Section 7 and, finally, some of the first SMASH science results are discussed in Section 8.

2. SURVEY STRATEGY

Figure 1 shows the region of the sky that is relevant to the Magellanic Clouds and the Magellanic Stream³², with the HI distribution in the top panel and the predicted stellar distribution of the Besla et al. (2013) model in the bottom panel. The DES footprint already covers one half of the LMC/SMC periphery as well as much of the trailing Magellanic Stream. The SMASH footprint was designed to cover the rest of the Magellanic periphery and the Leading Arm³³, but avoid the Milky Way mid-plane that could “contaminate” the data. A fully-filled survey would have been preferred, but to reach the sensitivity required to detect the predicted low surface brightness features would have required hundreds of nights and would be beyond the possibility of an NOAO survey proposal. We, therefore, decided to pursue a deep but partially-filled survey strategy as is shown in the top of Figure 1 (red hexagons). The SMASH fields map an area of $\sim 480 \text{ deg}^2$ but are distributed over (and probe the stellar populations of) $\sim 2400 \text{ deg}^2$ with a filling factor of $\sim 20\%$.

The DECam imager is composed of 62 chips (59 and a half are currently functional; CCDNUM 2, 61 and one amplifier of 31 are not producing useful science data) from Lawrence Berkeley National Lab (LBNL) arranged in a hexagonal pattern covering a field of view of $\sim 3 \text{ deg}^2$ and a width of $\sim 2^\circ$. The SMASH fields were chosen using an all-sky tiling scheme in which we laid down a uniform hex pattern of field centers with 1.7° separation between field centers with coordinates based on an Interrupted Mollweide projection. This spherical projection has low distortion, such that a uniform sampling in its coordinate system produces tiling with few areas of excessive overlap between fields. We then transformed the coordinates of the hex-based tiling to spherical coordinates, and rotated the coordinate system to place the

³² Also see Figure 10 which has more information on the SMASH fields including field names and calibration status.

³³ Note that even though the SMASH fields were designed to be complementary to the DES survey, the DES footprint changed over the last couple of years producing some overlap and gaps between the two surveys.

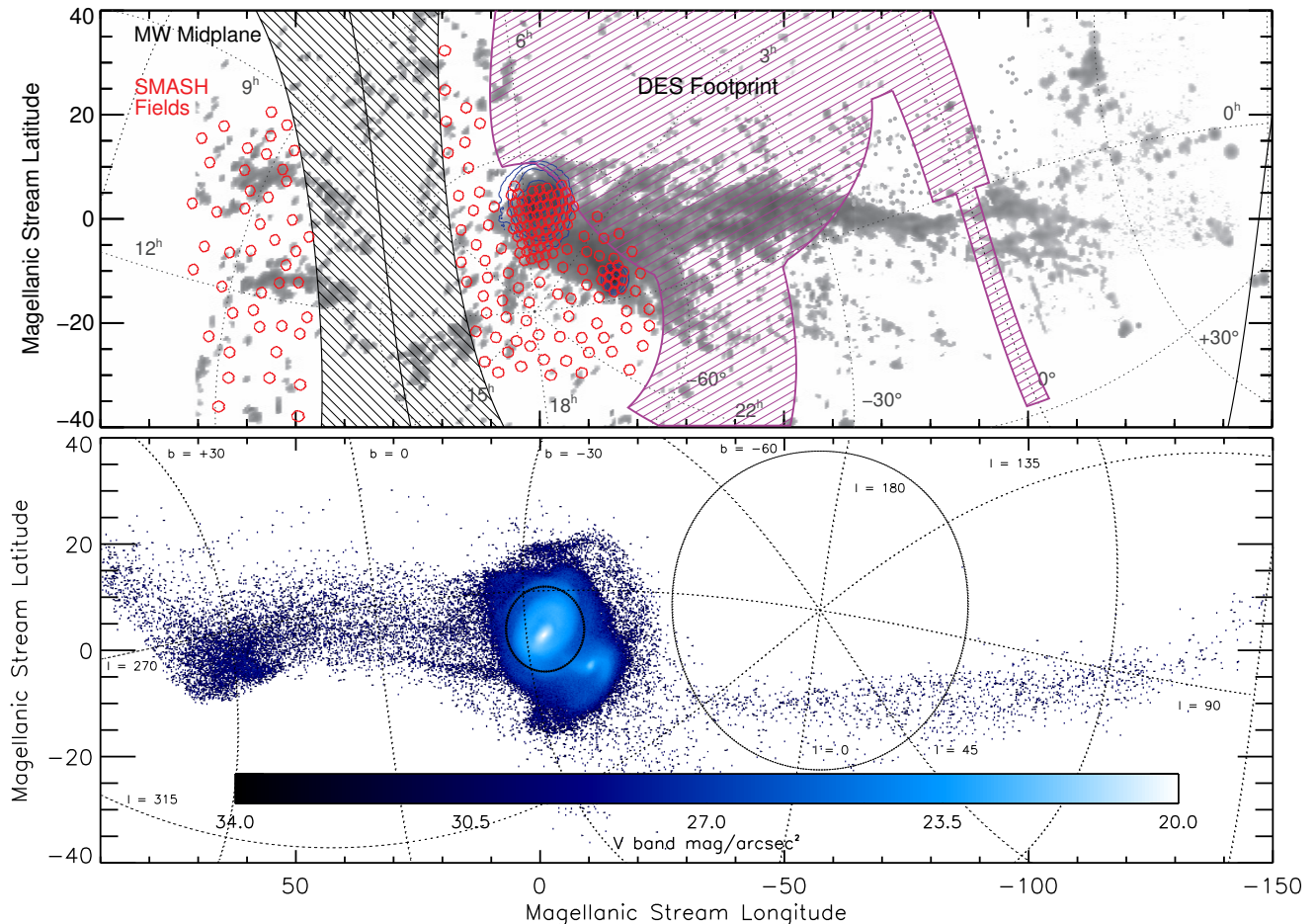


FIG. 1.— The region of the sky relevant to the Magellanic system in the Magellanic Stream coordinates system (Nidever et al. 2008). (Top) The observed H I column density of the entire 200° Magellanic Stream system (Nidever et al. 2010) is shown in grayscale, while the blue contours represent the 2MASS (Skrutskie et al. 2006) red giant branch starcounts. The open red hexagons are the SMASH survey fields (with the correct size and shape). The DES footprint is represented by the purple shaded region. The solid line represents the Galactic equator, the hashed region is a Galactic Zone of Avoidance region, and the dotted lines are an equatorial coordinate grid. (Bottom) The predicted V-band surface brightness (mag/arcsec^2) of the stellar component of the Magellanic system from Besla et al. (2013). The simulation predicts stellar structures out to large radii from the main bodies of the Magellanic Clouds (varying on small scales), and a higher stellar density in the Leading Arm than in the trailing Stream. In the absence of strong gas drag, the stellar and gas components are expected to be coincident. In this model the exact location of the debris is not tuned to match the observations, but the relative surface brightness of the various components is a robust prediction. A Galactic coordinate grid is shown in dotted lines.

seams and poles (southern pole of $[\alpha, \delta] = [10^\circ, -30^\circ]$) in areas outside of our survey area. The resulting tiling of the sky was nearly uniform over our survey area with $\sim 15\%$ areal overlap between neighboring fields to allow for good cross-calibration (although this was only used in our main body fields).

From this list of tiles we selected 154 fields by hand to uniformly sample the region of interest with a $\sim 20\%$ filling factor as well as fully cover the inner regions of the LMC and SMC. The full coverage tiling scheme and overlap was used so that, given more observing opportunities, we could more easily completely cover regions with interesting stellar populations later on, which is what we did for the outer LMC disk. Note that the final survey tiling scheme was created after the 2013, March 17–20 pre-survey run. Therefore, the positions of the 23 Leading Arm fields (Fields 153 – 175) that were observed on that run are not entirely consistent with those of the final tiling scheme, but the differences are not significant. The final list of SMASH fields with coordinates

in various systems is available in electronic version of Table 1 and the `data/smash_fields_final.txt` on the SMASHRED³⁴ repository.

3. OBSERVING STRATEGY AND OBSERVATIONS

The idea for SMASH was conceived during the NOAO “Seeing the Big Picture: DECam Community Workshop” in Tucson, AZ on August 18–19, 2011. We decided to submit a proposal for a Magellanic Clouds pilot project using Science Verification (SV) and Shared Risk (SR) time during the 2012B season. The goal of the successful project (SV:2012B-3005 and SR:2012-0416) was to ascertain the necessary filters and depth to attain the needed sensitivity to Magellanic stellar populations. Data were obtained in five fields at various distances from the Magellanic Clouds and included exposures in all five *ugriz* bands and to a depth ~ 1 mag deeper than we

³⁴ <https://github.com/dnidever/SMASHRED>

TABLE 1
SMASH FIELDS TABLE

Number	Name	RAJ2000	DEJ2000	RADEG	DEDEG	L _{MS} ^a	B _{MS} ^a
1	0010-6947	00:10:19.87	-69:47:40.56	2.58282	-69.794600	-19.56937	-13.84173
2	0018-7705	00:18:57.90	-77:05:00.23	4.74128	-77.083400	-12.11547	-15.01799
3	0023-7358	00:23:19.08	-73:58:08.04	5.82950	-73.968900	-15.14808	-13.94466
4	0024-7223	00:24:56.64	-72:23:08.15	6.23604	-72.385600	-16.67737	-13.38564
5	0044-7137	00:44:06.76	-71:37:45.84	11.02820	-71.629400	-16.91433	-11.74021
6	0044-7313	00:44:32.54	-73:13:31.79	11.13560	-73.225500	-15.38135	-12.28828
7	0045-7448	00:45:03.28	-74:48:14.76	11.26370	-74.804100	-13.85882	-12.82186
8	0050-8228	00:50:34.51	-82:28:26.40	12.64380	-82.474000	-6.36406	-15.28088
9	0101-7043	01:01:27.40	-70:43:05.51	15.36420	-70.718200	-17.19874	-10.09455
10	0103-7218	01:03:36.31	-72:18:54.36	15.90130	-72.315100	-15.66017	-10.63165

Full table is available in the electronic version of this paper.

^aMagellanic Stream coordinates defined in Nidever et al. (2008).

thought was necessary for our science goals. These data helped us evaluate various observing and survey strategies. Ultimately, it was determined that all five bands would give us the sensitivity needed to detect the predicted stellar populations in the Magellanic periphery and the Leading Arm. In addition, the *u*-band would allow us to determine photometric metallicities for the Magellanic main-sequence stars (e.g., Ivezić et al. 2008) which would be useful in determining the origin of any newly-found stellar populations.

After the pilot project, there was no call for survey proposals, so we proceeded to submit a regular NOAO proposal to look for stellar populations in the area of the Leading Arm (2013A-0411). To maximize the coverage we did not take *u*-band exposures for this observing run; however, the *u*-band exposures were obtained on later observing runs.

There was a call for survey proposals during the next semester, and we submitted a successful proposal for the SMASH survey of the Magellanic Cloud stellar populations (2013B-0440). We were originally awarded 30 DECam nights (with a 7/3 A/B semester split) and 14 0.9-m nights for calibration purposes over three years. The standard SMASH observing sequence for a science field is three 60 s exposures (with large, half chip offsets) in each band and three deep exposures with exposure times of 333 s (*u*), 267 s (*g*), 267 s (*r*), 333 s (*i*), and 333 s (*z*) with small $\sim 2''$ dithers. Each field takes about 110 min to observe including readout time and slewing. Each night exposures of four to five standard star fields (focusing on the York et al. 2000 SDSS equatorial region where data for all chips could be obtained simultaneously) were obtained with exposure times of 1 s in all *ugriz* bands as well as 10 s in *griz* and 60 s in *u*, but to save time this was later changed (half-way through the survey) to single exposures of 15 s in *griz* and 60 s in *u*.

Due to bad weather, poor seeing (we have seeing constraints of $\lesssim 1''$ for the central LMC/SMC main-body fields because of crowding), and the short B semester nights, the survey fell behind in the MC main-body regions. Therefore, after the first year we requested our 10 nights per year be split evenly between the A and B semesters (instead of 7/3 as before), and after the second year, we requested an additional three nights per semester in 2015B and 2016A. After our last year, we re-

quested a three night extension in 2016B to fill a “hole” in our coverage of the SMC periphery (near the south celestial pole) of 11 fields. Additional DECam nights were obtained through the Chilean TAC (PI: Muñoz; 2014 Jan. 21–28). Finally, after the discovery of the Hydra II Milky Way satellite in the SMASH data (Martin et al. 2015), we submitted a Director’s Discretionary Time proposal to obtain time-series data on Hydra II to study variable stars (2015 March 30–31).

On our very successful 2016 Feb 13–18 run, we finished all of the fields around the Magellanic Clouds that were observable and, therefore, we decided to observe some “extra” shallow fields around the LMC that would help reveal structures in the LMC disk (similar to those seen by Mackey et al. 2016 and Besla et al. 2016) and allow us to use the field overlaps to create a more homogeneously calibrated dataset around the LMC using an “übercal” technique (e.g., Padmanabhan et al. 2008). Two 60 s exposures in *griz* with a one half-chip dither between the pairs were obtained for these 40 fields (with field numbers between 184 and 243). The last SMASH observing run in the Leading Arm region (2016 May 8–12) was completely lost due to bad weather, and, therefore, the fields in that region were not completed.

SMASH was allotted 57 nights of DECam observations (on 63 separate nights with 12 of these being half nights) and 47 nights (or 75%) of useful data were obtained. All allocated observing for the SMASH survey has now concluded. The median seeing in *ugriz* is (1.22'', 1.13'', 1.01'', 0.95'', 0.90''), respectively, with a standard deviation of ~ 0.25 and the median airmass of all observations is 1.35. Useful exposures were obtained for 197 fields (158 deep fields) but 27 fields from our original survey plan remain unobserved due to poor weather conditions (mainly in the Leading Arm region). Table 2 shows all SMASH survey observing time including all time and data from non-NOAO sources (which are all combined as part of the SMASH dataset). More information about which nights were photometric are in the `smash_observing_conditions.txt` file (see Section 5.1 below).

3.1. 0.9-m Observations

TABLE 2
SMASH DECam AND 0.9-M OBSERVING RUNS

Date (nights)	Telescope	Source	Comments
Pre-Survey			
4-m Dec 11+12, 2012 (2)	4-m	Shared Risk	5 pilot fields
Mar 17–20, 2013 (4)	4-m	2013A-0411	23 fields (<i>griz</i>)
Aug 8+9, 2013 (2 part)	4-m	Time from Saha Bulge project	clear, 3 fields
Survey Year 1			
Sep 7–10, 2013 (4)	0.9-m	NOAO survey	bad weather, no data
Sep 11–13, 2013 (3)	0.9-m	Bought from SMARTS	bad weather, no data
Oct 21+22, 2013 (2 part)	0.9-m	Makeup for Sep 11–13	bad weather, no data
Jan 5–7, 2014 (3)	4-m	NOAO survey	0.5 night lost, 10 fields
Jan 12+13, 2014 (2)	0.9-m	Makeup for Oct 21+22	2 nights photometric, 4 fields calibrated
Jan 19+20, 2014 (2 half)	4-m	DD time	clear, <i>riz</i> for 6 fields
Jan 21–28, 2014 (8 half)	4-m	Chilean time	1 half night lost, 4 fields, 9 partials
Jan 29+30, 2014 (2 half)	4-m	DD time	clear, <i>ug</i> for 8 pre-survey fields
Feb 13, 2014 (1 part)	4-m	Engineering	clear, <i>riz</i> for 6 fields
Feb 14–23, 2014 (10)	0.9-m	NOAO survey	9 nights photometric, 30 fields calibrated
May 27–June 2, 2014 (7)	4-m	NOAO survey	lost 1 night, 21 fields observed, <i>ug</i> for 13 pre-survey fields, 3 extra fields
Survey Year 2			
Sep 25–Oct 1, 2014 (7)	0.9-m	NOAO survey	1 night photometric, 11 fields calibrated
Oct 11–12, 2014 (2)	4-m	Engineering	some globular cluster calibration data
Nov 21–23, 2014 (3)	4-m	NOAO survey	12 LMC/SMC main-body fields
Dec 17–18, 2014 (2)	4-m	NOAO survey	8 LMC/SMC main-body fields
Mar 13–18, 2015 (5)	4-m	NOAO survey	mostly clear, 21 finished, 4 partials
Mar 30–31, 2015 (2)	4-m	DD time	deep & high-cadence data of Hydra II
Apr 26–Mar 2, 2015 (7)	0.9-m	NOAO survey	4.5 nights photometric, 48 fields calibrated
Survey Year 3			
Oct 25+27, 2015 (2)	4-m	DD time	bad weather, no data
Nov 9, 2015 (1)	4-m	NOAO survey	clear, 4 fields
Nov 23, 2015 (1)	4-m	DD time	bad weather, long <i>riz</i> for 2 fields
Nov 27–29, 2015 (3)	0.9-m	Chilean time	9 fields calibrated
Dec 5+6, 2015 (2)	4-m	NOAO survey	8 fields, 7 are LMC/SMC main-body
Jan 1–6, 2016 (6)	4-m	NOAO survey	4 nights lost, 3 finished, 2 partials
Feb 13–18, 2016 (6)	4-m	NOAO survey	40 shallow LMC fields, 18 long fields
May 8–12, 2016 (5)	4-m	NOAO survey	bad weather, no data
Survey Year 4 – Extension			
Oct 29–31, 2016 (3)	4-m	NOAO survey	0.5 night lost, 8 fields

The CTIO 0.9-m telescope and Tek2K CCD camera were used to collect observations of SDSS standards and SMASH fields in order to provide an independent calibration of a portion of the DECam data, particularly for fields observed under non-photometric conditions with the 4-m telescope. The bulk of these observations were taken using CTIO’s SDSS *ugriz* filter set, while for three nights we used the borrowed DES PreCam *griz* filters for the sake of comparison.

The typical nightly observing plan in photometric weather was to observe several standard star fields from Smith et al. (2002) and from SDSS Stripe 82 and Stripe 10 (DR12; Alam et al. 2015) at the beginning and end of each night and every ~ 2 hours in between, and observe SMASH fields during the rest of the time. The Tek2K camera has a $13.5' \times 13.5'$ field of view, and so covered only the central portion of the SMASH fields. We did not offset the 0.9-m to cover the full DECam field of view, and so obtained calibration information only for the central DECam chips. Typical exposure times for the standard fields were 300 s (*u*), 20 s (*g*), 5 s (*r*), 10 s (*i*), and 15 s (*z*), while for the SMASH fields we took sets of five undithered exposures with individual exposure times of 600 s (*u*), 60 s (*g*), 60 s (*r*), 120 s (*i*), and

360 s (*z*). During non-photometric 0.9-m nights, we only took images of SMASH fields, and used short exposures of these fields taken on photometric nights to bootstrap the calibration of the non-photometric exposures. Table 2 also summarizes the 0.9-m observing runs.

Calibration data taken at the telescope consist of daily dome flats in *griz*, twilight sky flats in *ugriz*, exposures for the creation of a shutter shading map, and exposures for the creation of a bad pixel mask. The shutter shading calibration data consist of *r*-band dome flats observed while repeatedly opening the shutter for one second and closing it during the exposure, intermingled with normal dome flats taken with the same total exposure time as the shutter frames. The bad pixel mask data consisted of 100 0.1-s *r*-band dome flat exposures and a set of 6 *r*-band dome flats taken with levels equaling 75% of saturation.

4. DATA REDUCTION

The SMASH data reduction of the DECam data makes use of three separate software packages: (1) the NOAO Community Pipeline (CP; Valdes et al. 2014)³⁵ for in-

³⁵ http://www.noao.edu/noao/staff/fvaldes/CPDocPrelim/PL201_3.html also see the NOAO Data Handbook https://www.noao.edu/meetings/decam/media/DECam_Data_Handbook.pdf

strument signature removal, (2) PHOTRED³⁶ for PSF photometry, and (3) SMASHRED, custom software written for PHOTRED pre- and post-processing of the SMASH data.

4.1. Community Pipeline Reductions

The CP was jointly developed by the Dark Energy Survey Data Management (DESDM) team and NOAO (mainly by F. Valdes) to produce reduced images for the community. The CP performs the following operations on the data:

- Bias correction.
- Crosstalk correction.
- Saturation masking.
- Bad pixel masking.
- Linearity correction at both low and high count levels.
- Flat field calibration.
- Fringe pattern subtraction, for z and Y bands.
- Bleed trail and edge bleed masking and interpolation.
- Astrometric calibration of the image WCS with 2MASS as the astrometric reference catalog.
- Single exposure cosmic ray masking, by finding pixels that are significantly brighter than their neighbors.
- Photometric calibration using USNO-B1.
- Sky pattern removal. The “pupil ghost” and spatially varying background are subtracted.
- Illumination correction using a “dark sky illumination” image.
- Remapping to a tangent plane projection with constant pixel size.
- Transient masking with multiple exposures.
- Single-band coadding of remapped exposures with significant overlap.

The CP is run by NOAO staff on all the community DECam data and the reduced images are generally available a week or so after the end of an observing run and available via the NOAO Science Archive.³⁷ The CP produces instrumentally calibrated images (“InstCal”), remapped versions of InstCal (“Resampled”), and single-band coadded images (“Stacked”). For SMASH we use the InstCal images which come in three multi-extension (one per chip) and fpack³⁸ compressed FITS files per exposure: flux (“image”), weight/variance (“wtmap”), and quality mask (“qmask”).

³⁶ <https://github.com/dnidever/PHOTRED>

³⁷ <https://www.portal-nvo.noao.edu>

³⁸ <https://heasarc.gsfc.nasa.gov/fitsio/fpack/>

4.2. Pre-Processing with SMASHRED

The CP-reduced images are not in a format that is readable by DAOPHOT. Therefore, we run a SMASH pre-processing script (SMASHRED.PREP.PRO) on the CP images for each night before PHOTRED is run. This script performs the following steps:

1. Rename files in the old (“tu”) naming convention to the new (“c4d”) convention (the official NOAO archive file naming convention³⁹ was changed in early 2015).
2. Move standard star exposures to the “standards/” directory since they are processed separately from the science data.
3. Uncompress the FITS files, set “bad” pixels to 65,000, and write new FITS files for each chip.
4. Sort the exposures into PHOTRED “fields” based on the pointing and exposure times (short and long exposures are processed separately). Rename the files using the PHOTRED file naming convention (FIELD#-EXPNUM#_CHIP#.fits, e.g., F5-00507880_17.fits).
5. Download astrometric reference catalogs for each field and write separate reference catalog files for each chip FITS file.
6. Move files for each field into a separate directory (e.g., F8/, F9/, F10/, F11/).

The masks provide information on bad pixels, saturation, bleed trail, cosmic rays, and multi-exposure transients. There were some problems with the multi-epoch transient masking so we ignored that information in the mask. Any pixels that were affected by the other issues were set to a high value (65,000) so that PHOTRED/DAOPHOT would see these pixels as “bad”.

4.3. Nightly DECam PHOTRED Reduction

Accurate, point-spread-function (PSF) fitting photometry was obtained using the automated PHOTRED pipeline first described in Nidever et al. (2011). PHOTRED performs WCS fitting, single-chip PSF photometry as well as multi-exposure forced-PSF photometry using the DAOPHOT suite of programs (Stetson 1987, 1994). PHOTRED was run separately on each night. The short and long exposures of a field were run through PHOTRED separately (the former with a “sh” suffix added to their name) and multi-band image stacking and forced photometry were only performed on the long exposures. This was mainly because of issues with bright, saturated stars when stacking short and long exposures and the fact that the short exposures did not add much to the overall depth of the longer exposures. Note also that deep exposures of a field taken on different nights were processed separately and only combined during the calibration stage (see Section 5).

PHOTRED is based on methods and scripts developed by graduate students and postdocs in S. Majewski’s

³⁹ http://ast.noao.edu/sites/default/files/File_Naming_Conventions_v12.pdf

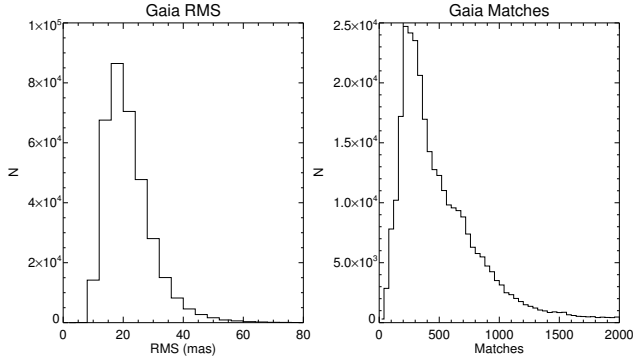


FIG. 2.— (Left) The distribution of rms values between the Gaia astrometric reference catalog and the SMASH DECam data for the final WCS (for the $\sim 350,000$ SMASH chips). (Right) The distribution of matches per chip between the SMASH and Gaia data with a median of ~ 500 matches per chip.

“halo” group at the University of Virginia (UVa) in the late 1990s and early 2000s (in particular J. Ostheimer, M. Siegel, C. Palma, T. Sohn & R. Beaton). PHOTRED fully automates these scripts (and some manual procedures) into a robust and easy-to-use pipeline. Most of the PHOTRED software was written by D.L. Nidever in 2008 while he was a graduate student at UVa and has been continually updated and improved since then. PHOTRED consists of IDL⁴⁰ driver programs wrapped around the DAOPHOT Fortran routines, but also includes some IRAF, Fortran and Unix shell scripts.

PHOTRED currently has 13 “stages”. Text-based lists are used for keeping track of inputs, outputs and failures and shuffling files from one stage to the next. This overall design was taken partly from the SuperMACHO “photpipe” pipeline (Rest et al. 2005; Miknaitis et al. 2007). The global parameters and optional settings (see the github repository for the full list) as well as the stages to be run are specified in the `photred.setup` setup file. The majority of the stages work on a chip-by-chip level (SPLIT-CALIB) and these chip-level catalogs are combined for the few final stages (COMBINE-SAVE). Although not all are used for SMASH, for completeness and future reference all of the stages are described in detail below.

4.3.1. RENAME

The headers are checked for all the required keywords (gain, read noise, time stamp, filter, exposure time, α/δ , airmass). The exposures are grouped into “fields” based on values in the “object” keyword in the header and renamed with the PHOTRED naming convention (FIELD#-EXPNUM#_CHIP#.fits). The PHOTRED short field names and full field names are saved in the `fields` file. This stage was skipped for SMASH since it is already performed by the `SMASHRED_PREP.PRO` pre-processing script.

4.3.2. SPLIT

If the FITS files are multi-extension files then these are split into separate FITS files per chip. This stage was also skipped for SMASH.

⁴⁰ The Interactive Data Language is a product of Exelis Visual Information Solutions, Inc., a subsidiary of Harris Corporation.

TABLE 3
DEFAULT PHOTRED OPTIONS FOR DAOPHOT

Option	Comment
TH = 3.5σ	Detection threshold
VA = 2	Quadratic spatial PSF variations
FI = $1 \times \text{FWHM}$	PSF fitting radius
AN = -6	Use lowest χ^2 analytical PSF model

4.3.3. WCS

The world coordinate system (WCS) for an image is created (or refined if it already exists in the header) by using an astrometric reference catalog and some information about the imager (pixel scale and orientation) and pointing (rough α/δ of the center of the image, normally from the Telescope Control System). The software (`WCSFIT.PRO`) performs its own simple source detection, sky estimation and aperture photometry of the image using routines from the IDL Astronomy User’s Library⁴¹. If a WCS does not already exist, then the reference catalog α/δ values are transformed roughly to the x/y cartesian coordinates of the image by using the exposure and image information provided. The reference sources are then cross-matched with the image sources by cross-correlating down-sampled “detection” map images of the two groups of sources. The peak in the cross-correlation image is used to obtain an initial measurement of the x/y offsets between the lists and the significance of the match. If a significant match is found then nearest-neighbor matching is performed with a large matching radius and the measured offsets. The matches are used to fit a four parameter transformation matrix (essentially translation, rotation and scale) and a second round of improved nearest-neighbor matching. The final matches are used to perform fitting of the four CD#_# and two CRVAL# parameters of the WCS. The software does not create or modify existing higher-order distortion terms but uses if they already exist in the header (e.g., for DECam the existing PV#_## TPV distortion terms are used).

By default, the SMASHRED pre-processing used USNO-B1⁴² (Monet et al. 2003) as the astrometric reference catalog, and sometimes 2MASS or UCAC4 (Zacharias et al. 2013). The rms of the residuals of the astrometric solutions with these catalogs gave values of ~ 270 mas. After the first Gaia data release (Gaia Collaboration et al. 2016), the WCS-fitting software was rerun with Gaia as the astrometric reference and the resulting FITS header (with the improved WCS) saved in a separate text file (`gaiawcs.head`) for each image. The astrometric solutions were dramatically improved, with a resultant rms of only ~ 20 mas (see Figure 2).

4.3.4. DAOPHOT

This stage detects sources in the single exposure images, constructs the PSF, and uses it to measure PSF photometry with ALLSTAR. There are several steps:

1. **PSF FWHM Estimate:** Since DAOPHOT requires an estimate of the PSF FWHM (full width

⁴¹ <http://idlastro.gsfc.nasa.gov>

⁴² <http://tdc-www.harvard.edu/catalogs/ub1.html>

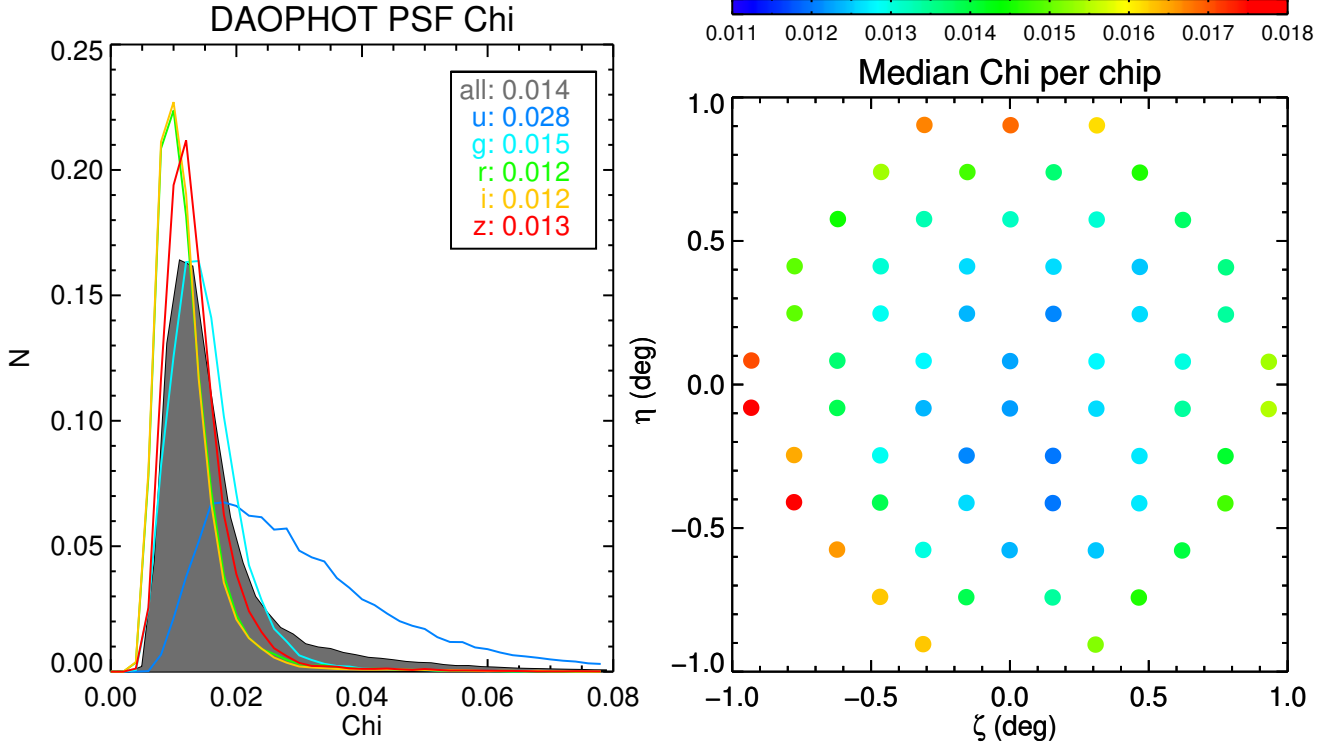


FIG. 3.— (Left) The distribution of DAOPHOT PSF “chi” values (relative root-mean-square of the analytic PSF residuals) for the $\sim 350,000$ SMASH chips broken down by band. The median values per band are given in the legend. (Right) The median chi value per chip (over all bands) as they appear in the focal plane.

at half maximum, or seeing), a custom IDL routine (`IMFWHM.PRO`) with independent algorithms is used to make this estimate. The routine detects peaks in the image 8σ above the background (although this is lowered if none are detected) and keeps only those peaks having the maximum value within 10 pixels of the peak position and have two or more neighboring pixels that are brighter than 50% of the peak’s flux (to help weed out cosmic rays). The routine then finds the contour at half-maximum flux in a 21×21 sky-subtracted sub-image centered on the peak and uses it to measure an estimate of the FWHM ($2 \times$ the mean of the radius of the contour) and the ellipticity of the contour. In addition, the total flux in the subimage and a “round” factor (similar to the DAOPHOT version) using marginal sums are computed. These metrics are then used to produce a cleaner list of sources ($\text{FWHM} > 0$, $\text{round} < 1$, $\text{ellipticity} < 1$ and $\text{flux} < 0$) on which two-dimensional Gaussian fitting is performed and more reliable metrics are computed. The final list of sources is selected by cuts on the new metrics and the distributions of semi-major axis, semi-minor axis and χ^2 (selected sources must lie within the dominant clustering of these parameters for all sources). The final FWHM and ellipticity are then computed from these sources using robust averages with outlier rejection. This FWHM value is then used in the next step to set the DAOPHOT input options.

2. **DAOPHOT option files:** Both DAOPHOT and ALLSTAR require option files (`.opt` and `.als.opt`

respectively). Some of the most important default settings are shown in Table 3.

For some very crowded fields (e.g., Field35 and Field46) the default settings produced suboptimal results and, therefore, linear PSF spatial variations ($\text{VA}=1$) and a smaller fitting radius ($\text{FI}=0.75 \times \text{FWHM}$) were used. The affected nights are 20141123, 20141217, 20151205 and 20151206.

3. **Common sources list:** Early on in the development of PHOTRED there were issues with constructing good PSFs for the deep (280 s), intermediate-band DDO51 observations for the MAPS survey (Nidever et al. 2011, 2013, which was the main motivation for writing PHOTRED). This was because there were a lot of point-like cosmic rays that overwhelmed the small number of real sources and made it difficult to create a good PSF source list just by culling via morphological parameters. To deal with this problem, PSF sources were required to be detected in multiple images (across all filters) to make sure they were real objects. In this step, a “common sources list” is constructed for each file and later used as the starting point to select PSF stars. In the DECam data, the original issue is not as much of a problem because of the broad-band filters and because the cosmic rays in the LBNL detectors tend to be more linear and less point-like in shape. However, we have continued to use the common sources option in the DAOPHOT stage for SMASH.

4. **Detection:** Sources are detected in the images

with **FIND**, and aperture photometry is determined with **PHOTOMETRY** with an exponential progression of apertures from 3 to 40 pixels and sky radius parameters of 45 (inner) and 50 (outer) pixels.

5. **Construct PSF:** The PSF is constructed with an iterative procedure for culling out “suspect” sources. The initial list of 100 PSF sources is selected using **PICK** from the common source list (or the aperture photometry file if the common source option was not used) and a morphology cut is applied ($0.2 \leq \text{sharp} \leq 1.0$; using the sharp produced by **FIND**) to remove extended objects. The list is then iteratively cleaned of suspect sources. At each iteration a new PSF is constructed with **PSF** using the new list and **DAOPHOT** prints out the “chi” value (root-mean-square residual of the stellar profile from the best-fitting analytic model) for each star and flags any outliers (? and * for 2 and 3 times the average scatter, respectively). The flagged outliers and any sources with $\text{chi} > 0.5$ are removed from the list and the procedure is started over again until no more sources are rejected.

After the list has converged, sources neighboring the PSF sources (using **GROUP**) are removed from the image (using **SUBSTAR**). A new PSF is constructed from this “neighbors subtracted” image and a similar iterative loop is used to remove PSF outlier sources. The median number of PSF stars used per chip is ~ 80 .

The default **PHOTRED** setting is to allow **DAOPHOT** to pick the analytic function that produces the lowest chi value. The most commonly used function (77% of the PSFs) is the four-parameter “Penny”, which is the sum of a Gaussian and Lorentz function. The second most common function (20% of the PSFs) is a Moffat function with a power law exponent of $\beta=3.5$.

6. **Run ALLSTAR:** **ALLSTAR** is run to perform simultaneous PSF fitting on all the detected sources in the image using the constructed PSF. The default **PHOTRED** setting is to allow **ALLSTAR** to recentroid each source. **ALLSTAR** is also run on the “neighbors subtracted” images to obtain PSF photometry for the PSF stars that are later used to calculate an aperture correction. **ALLSTAR** outputs x/y centroids, magnitudes with errors, sky values, as well as chi and sharp (which describes how much broader the profile of the object appears compared to the profile of the PSF) morphology parameters (.als file).

One of the failure modes for a file in this stage is not to have enough PSF stars after the cleaning to constrain the solution. In these cases the PSF spatial variation value (**VA**) is lowered in the option file by hand and **DAOPHOT** rerun. This solves the failures in the large majority of cases. For the small number of files where this also fails, we select PSF sources by visual inspection. The software will be modified to avoid these problems in the future by starting with a simple, constant analytic PSF and slowly add more complexity if it is needed.

Figure 3 shows the histogram of **DAOPHOT** analytic PSF chi values broken down by band. The *griz* chi values are tightly peaked around ~ 0.012 (or 1.2%) while the *u*-band values are a factor of $2\times$ larger. The higher *u*-band values are because the S/N of the PSF stars are on average lower, which gives rise to larger scatter in the residuals from photon noise. The right-hand panel of Figure 3 shows the median chi value per chip (across all exposures) as they appear on the sky, indicating that the analytic first approximations are slightly poorer for the chips on the periphery of the focal plane, possibly due to optical distortions or non-conformity of the detectors to the focal plane. Note that any systematic differences between the “true” PSF and the analytic first approximation go into **DAOPHOT**’s PSF empirical look-up table of corrections, so the final rms of the PSF residuals will actually be smaller than the chi values. Figure 4 shows diagnostic thumbnails of median-combined relative flux residuals from PSF-subtracted images of many bright stars. The PSF relative flux error is of the order of $\sim 0.3\%$ with very little systematic structure left in the medianed residual image indicating that the PSFs are of high quality.

4.3.5. MATCH

The sources in the **ALLSTAR** photometry catalogs from the **DAOPHOT** stage are cross-matched and combined with the files for each chip being handled separately (i.e., all the chip 1 files are cross-matched together and the chip 2 files are cross-matched together, etc.). Astrometric transformations between the frames (using the x/y cartesian coordinates) and a reference frame (which is chosen based on the longest exposure time frame in the **filtref** band) are computed (in similar manner to what **DAOMATCH** achieves). The WCSs in the FITS headers are used to calculate an initial estimate of the transformations. If this fails, then a more general matching routine is run that uses a cross-correlation technique of a down-sampled “detection” map image between the two source lists (as described above in Section 4.3.3). Once all the transformations are in hand, **DAOMASTER** is used to iteratively improve the transformations (written to .mch file) and cross-match, and, finally, combine all of the photometry (per chip) into one merged file (the .raw file).

4.3.6. ALLFRAME

PSF photometry can be improved by using a stacked image for source detection and then holding the position of the sources fixed while extracting PSF photometry from each image. The improvement of this “forced” photometry over regular PSF photometry performed separately from each image comes from the reduced number of free parameters (i.e., the positions). **PHOTRED** makes use of the **DAOPHOT ALLFRAME** (Stetson 1994) program to perform the forced photometry. The **ALLFRAME** stage processes each group of chips separately (e.g., chip 01 files separately from chip 02 files, etc.).

This stage performs several separate tasks:

1. **Construct multi-band coadd:** A weighted average stack is created of all the images. First, the

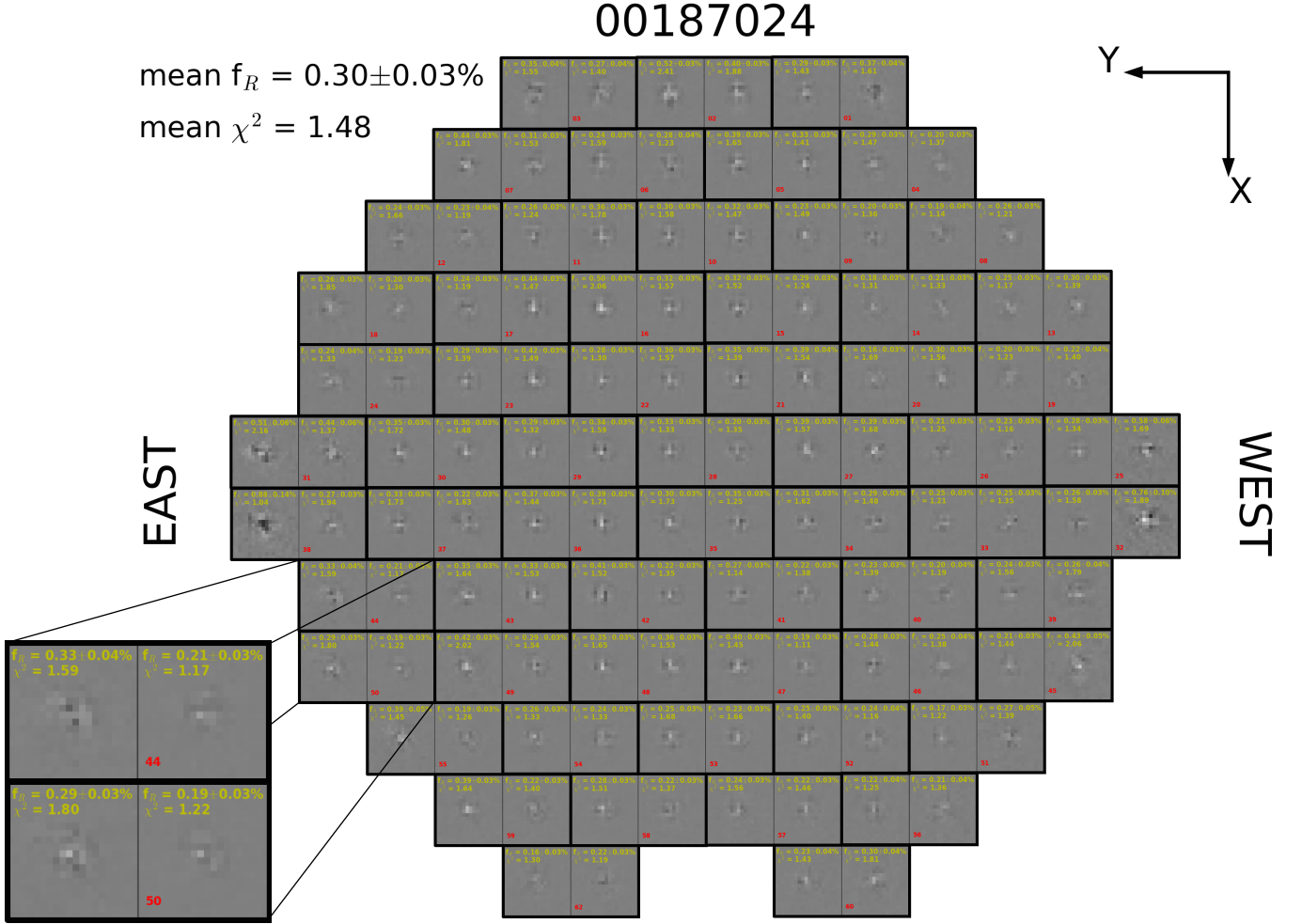


FIG. 4.— PSF quality assurance figure for the full focal plane of a single exposure (EXPNUM=00187024) and a blow-up of two chips in the lower-left. Each square image shows the relative residuals in the PSF-subtracted image (relative to total flux in the PSF model) medianed across ~ 30 high S/N stars (not necessarily PSF stars) per half-chip. Each horizontal rectangle represents one chip of an exposure, and the two squares in the rectangle show the relative residuals for one half of the chip. The relative absolute residuals and the uncertainties (using propagation of errors from the noise in each image) as well as the χ^2 for each half-chip are shown in yellow. The range of the greyscale is $\pm 0.2\%$ and the chip number (CCDNUM) is shown in red. Average values for the entire exposure are in the upper-left.

relative flux scaling, sky level, and weights are computed for all the images. The weights are essentially the S/N and are based on sources detected in all of the images (if no sources are detected in all the images, then a bootstrap approach is used to tie the images to one another). Second, images are transformed to a common reference frame. The original code only applied x/y translations to the images. However, this was insufficient for larger dithers where the higher-order optical distortions become important and the software was rewritten to fully resample the images onto the final reference frame. The type of transformation used can be found in the ALFILETYPE column (“ORIG” or “WCS”) of the final chips catalog/table. Finally, the images are average combined using the IRAF routine IMCOMBINE with bad pixel masking and outlier rejection (sigma clipping). The detector gain recorded in the image header is maintained because the images are scaled to the reference exposure. However, new read noise and sky

values⁴³ for the combined image (`_comb.fits`) are computed using the weights, scalings and sky values. It is challenging to preserve the fidelity of bright stars when combining deep and shallow exposures. This is one reason why it was decided to process short and long SMASH exposures separately in PHOTRED.

2. **PSF construction:** The PSF of the combined image is constructed using the same routine as in the DAOPHOT stage.
3. **Iterative source detection:** Source detection is performed iteratively in two steps. (1) Detect new sources in the working image (PSF subtracted after the first iteration) with Source Extractor (SExtractor, which works well for detecting faint sources; Bertin & Arnouts 1996) and incorporate these new detections into the master source

⁴³ Sky is needed in the combined images because DAOPHOT uses it as part of its internal noise model.

list. (2) ALLSTAR is run on the original image (with the previously-found PSF) using the current master source list and all sources that converge are subtracted. This two-step process is repeated for the desired number of iterations (`finditer` option in `photred.setup`). The ALLSTAR output from the last iteration is used as the final master source list (`_comb_allf.als`). The default detection settings for SExtractor are: use a convolution filter, $>1\sigma$ detection threshold, and a minimum area of 2 pixels per source. For SMASH only two iterations were used since we found that further iterations produced mainly spurious new detections.

4. **Run ALLFRAME:** ALLFRAME is run on all the images using their respective PSFs and the master source list constructed in the previous step. ALLFRAME uses the coordinate transformations between images from the `.mch` file (in the MATCH stage), but computes its own small, high-order geometric adjustments (we use the option of 20 terms or cubic in x and y) to these during the fitting process (it slowly adds in the higher orders to keep the solutions constrained). We allow a maximum of 50 iterations in ALLFRAME after which it outputs catalogs (`.alf`) with x/y coordinates (in that image's reference frame), photometry with errors and chi and sharp morphology parameters.

After ALLFRAME has finished, the results for the individual images are combined and the SExtractor morphology parameters are added to the final catalog (`.mag` file).

It is possible to skip the ALLFRAME stage for certain fields by specifying them in the `alfexclude` option of the `photred.setup` file. This option was used for the short SMASH exposures.

4.3.7. APCOR

The DAOPHOT program DAOGROW (Stetson 1990) is used to produce growth-curves for each band and night separately. These are used to produce “total” photometry (including the broad wings) for the bright PSF stars for each chip. These values are then compared to the PSF photometry values for the PSF stars (from neighbor subtracted images) produced in the DAOPHOT stage to compute an average aperture correction for each chip. These values are all stored in the `apcor.lst` file and used later in the CALIB stage.

4.3.8. ASTROM

The WCS in the FITS header is used to add the α and δ coordinates for each object to the catalog.

4.3.9. CALIB

The photometry is calibrated using the transformation equations given in the transformation file specified in `photred.setup` (e.g., `n1.trans`). The equations in the file can pertain to various levels of specificity: (1) only the band is specified, (2) the band and chip are specified, or (3) the band, chip and night are specified. The terms in the transformation file are zero-point, extinction, color, $\text{extinction} \times \text{color}$, and $\text{color} \times \text{color}$, along with their uncertainties. Besides these corrections the

photometry is also corrected for the exposure time and the aperture correction (for that chip).

Because the *calibrated* color is used for the color term, the software uses an iterative method to calibrate the photometry (using an initial color of zero). A weighted average value from all exposures is used for the magnitude in the other band to construct the color (if multiple exposures in that band were taken) but not for the band being calibrated (the value for that exposure is used). Also, a color of zero is used for objects for which a good color cannot be constructed. The loop to derive the true source color continues until convergence (all magnitude differences are below the 0.1 mmag level or 50 iterations, whichever is first).

Calibrated photometry for each exposure (e.g., G2, Z4) is given in the output file and, optionally, the average magnitudes per band (e.g., GMAG, ZMAG) and the instrumental magnitudes for each exposure (e.g., I_G2, I_Z4). Because for SMASH a global calibration strategy was adopted, all of the values in the transformation file were set to zero so that the photometry was only corrected for the exposure time and aperture corrections.

4.3.10. COMBINE

The individual chip catalogs are combined to create one catalog for the entire field. Sources detected in multiple chips (from dithered exposures) are combined and their photometry combined. The default matchup radius is $0.5''$ (~ 2 pixels).

4.3.11. DEREDDEN

Schlegel, Finkbeiner & Davis (1998, SFD) $E(B - V)$ extinction values for each source are added as a separate column in the final, combined catalog. Extinction ($A[X]$) and reddening ($E[X - Y]$) values for the bands and colors specified in the `photred.setup` setup file (using $A[X]/E[B - V]$ values from the given `extinction` file) are also added to the catalog. The *ugriz* reddening coefficients from Schlafly & Finkbeiner (2011) were used for SMASH.

4.3.12. SAVE

The final ASCII catalog is renamed to the name of the field (e.g., F5 is renamed to Field62) and a copy is created in the IDL “save” and FITS binary table formats. In addition, a useful summary file is produced with information on each exposure and chip for that field.

4.3.13. HTML

This stage creates static HTML pages to help with quality assurance of the PHOTRED results. Quality assurance metrics are computed and plots created for the pages. This stage was skipped for SMASH since custom quality assurance routines were written.

4.4. Processing of Standard Star Data with STDRED

The southern sky that SMASH is observing has not been well covered with *ugriz* CCD imaging, which means that it is not possible to calibrate our photometry with existing catalogs (in the same area of the sky) as can be done in the north by use of SDSS and Pan-STARRS1

TABLE 4
0.9-M PHOTOMETRIC TRANSFORMATION EQUATIONS (SDSS FILTER SET)

Band	$(ABCDE)_1$	$(ABCDE)_2$	$(ABCDE)_3$	$(ABCDE)_4$	$(ABCDE)_5$	$(ABCDE)_6$	$(ABCDE)_7$
14 – 23 Feb 2014							
<i>u</i>	1.001 ± 0.002	0.51 ± 0.02	0.0	0.0	0.0	-0.034 ± 0.004	4.59 ± 0.04
<i>g</i>	0.997 ± 0.001	0.19 ± 0.01	0.0	0.0	0.0	0.009 ± 0.011	2.66 ± 0.03
<i>r</i>	0.995 ± 0.001	0.11 ± 0.01	0.0	0.0	0.0	-0.022 ± 0.007	2.67 ± 0.02
<i>i</i>	0.995 ± 0.002	0.06 ± 0.01	0.0	0.0	0.0	-0.017 ± 0.014	3.13 ± 0.03
<i>z</i>	0.998 ± 0.001	0.07 ± 0.02	0.0	0.0	0.0	0.040 ± 0.011	3.95 ± 0.02
25 Sep – 2 Oct 2014, 26 Apr – 3 May 2015, and 27 – 29 Nov 2015							
<i>u</i>	1.0	0.49 ± 0.02	0.0	0.0	0.0	-0.034	4.17 ± 0.29
<i>g</i>	1.0	0.18 ± 0.01	0.0	0.0	0.0	0.005	2.51 ± 0.31
<i>r</i>	1.0	0.10 ± 0.01	0.0	0.0	0.0	-0.028	2.49 ± 0.21
<i>i</i>	1.0	0.06 ± 0.01	0.0	0.0	0.0	-0.026	2.91 ± 0.12
<i>z</i>	1.0	0.06 ± 0.01	0.0	0.0	0.0	0.022	3.72 ± 0.05

(Chambers et al. 2016) data. Therefore, we must use the traditional techniques of calibrating our data with observations of standard star fields (on photometric nights) and extra calibration exposures (for non-photometric nights). We use standard star data taken in the SDSS footprint along the celestial equator and downloaded “reference” catalogs via CasJobs⁴⁴ from the SDSS DR12 (Alam et al. 2015). These observations generally provided several thousands of standard star measurements per exposure.

To reduce the DECam standard star exposures we use the STDRED pipeline, which is a sister package to PHOTRED and works in a similar manner. The same SMASHRED_PREP.PRO pre-processing script is used to uncompress, mask and split the CP-reduced images and download the astrometric reference catalogs per field. The main STDRED steps that are used by SMASH are:

- WCS: Fits the chip WCS using the astrometric reference catalog.
- APERPHOT: Detects sources and performs aperture photometry.
- DAOGROW: Calculates aperture corrections via curves of growth and applies them to the aperture photometry.
- ASTROM: Adds α/δ coordinates to the photometric catalog.
- MATCHCAT: Cross-matches the observed catalog with the reference catalog and for matches outputs merged information from both catalogs.
- COMBINECAT: Combines all of the matched photometry for a given filter.
- FITDATA: Fits photometric transformation equations (with zero-point, color, and extinction terms) for each filter using all of the data.

The standard star exposures from each DECam run are processed with STDRED in their own directory. The process of deriving the final SMASH DECam photometric transformation equations are described in Section 5.1.

4.5. Reduction of the 0.9-m data

4.5.1. Image processing

We used the NOAO/IRAF QUADRED package, custom IDL programs, and other software to process the images from the 0.9-m observations. The basic steps of this processing are:

1. Electronic crosstalk correction, using custom software to measure and correct for the electronic ghosting present in the images when read through multiple amplifiers.
2. Correction for electronic bias using the CCD’s over-scan region and bias frames.
3. Trimming of the images to the illuminated area.
4. Derivation of the exposure time-dependent illumination map caused by the opening and closing of the camera’s iris shutter using dome flat observations designed for the purpose, and application of this shutter shading correction to the observed images.
5. Derivation of flat field frames from twilight sky images and application to the object frames.
6. Derivation of a bad pixel mask from dome flat observations designed for the purpose, with bad pixel correction applied to the object frames.
7. Derivation of dark sky flats (*ugri*) and fringe frames (*z*) by stacking and filtering the deep sky observations taken throughout each observing run, followed by division by the dark sky flats (*ugri*) and subtraction of fringe features (*z*) for all object frames.
8. Use of the code library from <http://astrometry.net> (Lang et al. 2010) to populate the object image headers with World Coordinate System (WCS) solutions.

⁴⁴ \protect<http://casjobs.sdss.org>

4.5.2. Photometry

We performed photometry on the 0.9-m observations of SDSS standards and SMASH target fields with a pipeline based on the DAOPHOT software suite (by K.O., separate from PHOTRED/STDRED). In short, we used DAOPHOT to measure aperture-based photometry of the standard star frames, with a smallest aperture of 6'' diameter (~ 15 pixels) and a largest aperture of 15'' diameter (~ 38 pixels). We used DAOGROW to measure the growth curve based on the aperture measurements and to extrapolate the total magnitudes of the standard stars. These total magnitudes were used to derive the photometric transformation equations from the standard star observations. We also measured PSF photometry of the SMASH target fields and the standards using DAOPHOT and ALLSTAR. We derived PSFs from the images using as many as 200 point sources per image, using an iterative method to remove neighbors from the PSF stars and to improve the PSF estimation. We applied aperture corrections to the PSF photometry by comparing the PSF measurements with the total magnitudes from DAOGROW and fitting for the residuals with second-order polynomial function in x and y . These aperture-corrected PSF magnitudes were used as the basis of our standard magnitudes for the SMASH fields, while for standard fields they served as a consistency check between the aperture and PSF-based procedures, as described further below.

4.5.3. Derivation of 0.9-m transformation equations

Using the total magnitudes from DAOGROW, we explored fits to equations of the form:

$$\begin{aligned} u_{\text{obs}} &= A_1 u + A_2 X + A_3 x + A_4 y + A_5 t + A_6(u - g) + A_7 \\ g_{\text{obs}} &= B_1 g + B_2 X + B_3 x + B_4 y + B_5 t + B_6(g - r) + B_7 \\ r_{\text{obs}} &= C_1 r + C_2 X + C_3 x + C_4 y + C_5 t + C_6(g - r) + C_7 \\ i_{\text{obs}} &= D_1 i + D_2 X + D_3 x + D_4 y + D_5 t + D_6(r - i) + D_7 \\ z_{\text{obs}} &= E_1 z + E_2 X + E_3 x + E_4 y + E_5 t + E_6(i - z) + E_7, \end{aligned}$$

where $u_{\text{obs}}, g_{\text{obs}}, r_{\text{obs}}, i_{\text{obs}}, z_{\text{obs}}$ are instrumental magnitudes, $ugriz$ are standard SDSS magnitudes drawn from Smith et al. (2002) and from SDSS DR12 (Alam et al. 2015), X is the airmass, x and y are pixel positions on the detector, and t is time of observation during the night.

We fit this set of equations first to the data taken on the almost entirely photometric run from 14 – 23 Feb 2014. Table 4 shows the best-fit coefficients. While we fit the transformation equations independently on each of the ten nights, we show only the average coefficients and their standard deviations in the table, as values were in all cases consistent across the nights. From our fits, we found no evidence for strong pixel position-dependent or time-dependent terms. We did, however, find evidence for a small magnitude-dependent scale factor of ~ 0.1 – 0.5% , which may point to a small non-linearity with the Tek2K CCD.

We next explored fits to the equations for the observing runs 25 Sep – 2 Oct 2014, 26 Apr – 3 May 2015, and 27 – 29 Nov 2015. These runs were complicated by variable weather conditions, work on the camera electronics that changed the gain setting of the CCD, and by a temporary change from the CTIO SDSS $griz$ filter set to the PreCam $griz$ filter set that more closely matches the filter set

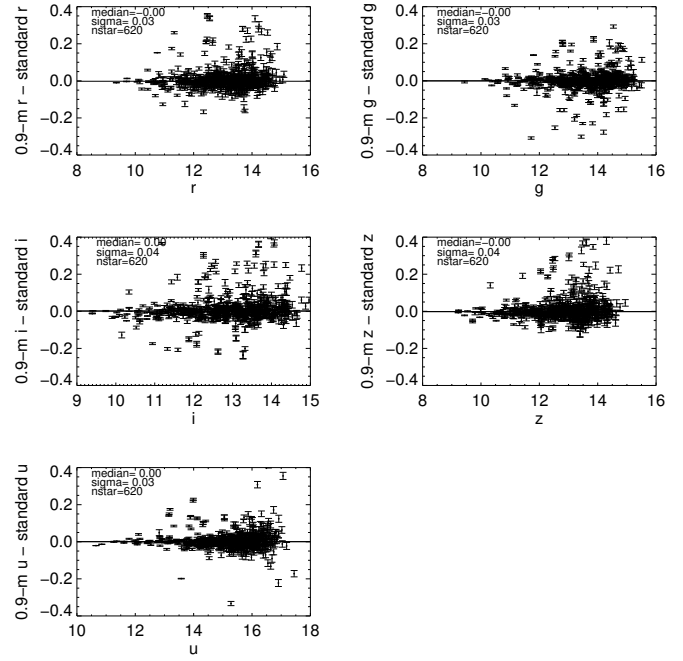


FIG. 5.— Residuals of the 0.9-m photometry relative to the standard star data versus magnitude for the $ugriz$ bands. Statistics for the residuals are in the upper left-hand corner indicating rms values of 0.03–0.04 mag.

TABLE 5
0.9-M PHOTOMETRIC COLOR TERMS
(DES PRECAM FILTER SET)

Band	$(ABCDE)_6$
30 Apr – 3 May 2015	
u	-0.033 ± 0.01
g	0.020 ± 0.001
r	-0.068 ± 0.001
i	-0.063 ± 0.001
z	-0.026 ± 0.002

used by DECam. For these observations, we fit the SDSS and PreCam sets separately. For each filter set, we first used all of the nights observed with that set to measure the color term coefficients. To do this, we allowed the zero point for each frame to be fit independently, which removes all other variables from consideration other than the color term; this allowed us to use standards taken on non-photometric nights to constrain the color term. We then fixed the color term coefficients to these fitted values, and for the photometric nights fit for the remaining coefficients on a per night basis. For these fits, we found no evidence for pixel position-dependent, time-dependent terms, or, in contrast to the Feb 2014 observations, a magnitude-dependent scale term. Table 4 shows the fitted coefficients for the SDSS filters, where the larger standard deviation in the tabulated zero point reflects the large span of time over which the observations were taken. Figure 5 shows the photometric residuals for the standard star fields. Table 5 shows the color terms for the DES PreCam filter set, for which we

did not derive full transformation equations because of weather that was not completely photometric. We found some significant differences between the DES PreCam and SDSS color terms, particularly for the r , i , and z filters, as is to be expected from the differences in the bandpasses. The color terms are not, however, identical to those measured with DECam, which we ascribe to differences in the PreCam bandpasses compared to DECam, as well as to differences in the telescope and detector response functions. In the end, we did not use the PreCam data for calibration, other than to verify that using a filter set that is a closer match to those used with DECam reveals systematic differences with the SDSS filters.

5. CALIBRATION

5.1. Derivation of DECam Photometric Transformation Equations from Standard Star Data

To produce the highest-quality and most uniform calibration we decided to write new custom software to determine the DECam photometric transformation equations using all of the standard star data together. Transformation equations of the following form were used:

$$m_{\text{obs}} = m_{\text{cal}} + \text{ZPTerm} + \text{COLTerm} \times (\text{color}_{\text{cal}}) + \text{AMTerm} \times X$$

where ZPTerm is the zero-point term, COLTerm is the color term, $\text{color}_{\text{cal}}$ is the calibrated color (which includes the band being calibrated), AMTerm is the extinction term, and X is the airmass.

The new software (SOLVE_TRANSPHOT.PRO) has several options for what variables to fit or hold fixed (zero-point, color, extinction, and color \times extinction terms) and over what dimensions (e.g., night and chip) to average or “bin” values. At first all variables (zero-point, color and extinction terms) were fit separately for each night and chip combinations to see how much the terms vary and over what dimensions.

Color: We found that the color terms vary from chip to chip (at the ~ 0.01 mag level as also noted on the DECam Calibration webpages⁴⁵; see the left-hand panel of Figure 6), but they appear to be temporally stable (see the bottom panel of Figure 6). Therefore, we fit the (linear) color terms for each chip separately by taking a robust average over all photometric nights.

No evidence for systematics was found in the color residuals of $g/i/z$ indicating there was no need for higher order color terms. For u -band there are systematics in the residuals (consistent across all fields) that would require higher order terms to fit. This is largely because of the different throughput curves for the SDSS and DECam filters. We decided not to add higher order terms as these could adversely affect very blue or red objects (where the solution is not well constrained). However, to determine a uniform and reliable zero-point we decided to fit the shape in the residuals and remove this pattern from the observed data at the very beginning of the procedure. In addition, we restricted the color range to $1.0 < u-g < 2.5$. After this correction and color restriction are applied the residuals are flat. We similarly restrict the color range for r band ($g-r < 1.2$) because the correlation between SDSS and DECam r -band magnitudes becomes non-linear for redder stars due to the difference in the throughput curves.

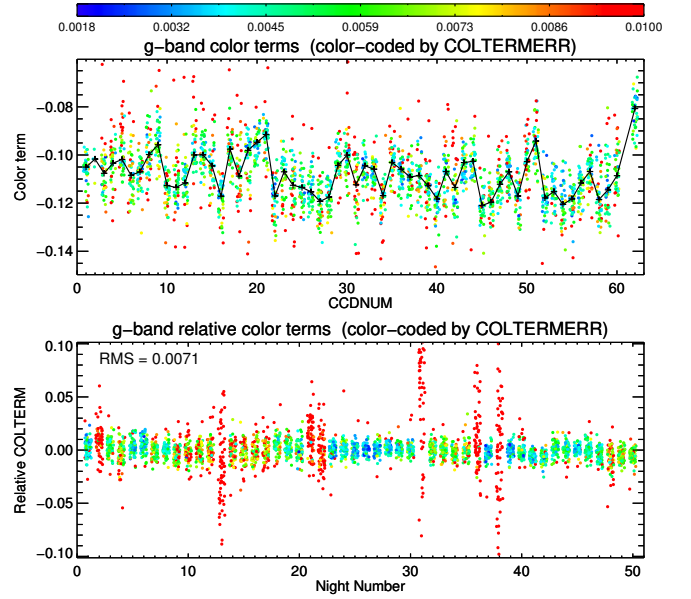


FIG. 6.— The g -band color terms of the DECam photometric transformation equations. (Top) Dependence on chip number and (Bottom) temporal dependence (night number is a running counter). The nights with large scatter are non-photometric nights.

Extinction: An appreciable number of nights had a small range in airmass for the standard star observations that produced unreliable extinction term measurements. Therefore, for these nights we calculated a weighted (by uncertainty and time difference) average of the nightly extinction terms for the four closest neighboring good nights. Similarly, for nights with larger airmass ranges, we improve the accuracy by refitting the extinction term using the individual data points from the four closest good neighboring nights (but these must be within 30 nights). Finally, we found that there was no appreciable color \times extinction dependence and, therefore, these terms were not included in the fits.

Zero-point: We tried separating the zero-points into nightly zero-points and relative chip-to-chip (for each band but constant with time) zero-point offsets, considering that although the zero-point can change nightly, due to transparency and extinction variations, the zero-points of one chip to another (in a given band) should remain the same. We found, however, that the scatter in the relative chip-dependent zero-points over the many nights was somewhat higher than was anticipated (but still small at ~ 0.01 mag) and we obtained better results by fitting a zero-point for each night and chip combination. Therefore, we adopted the latter strategy and “abandoned” the relative zero-points (although they are computed and saved in the final output file).

Photometric nights are determined by seeing if the observers noticed any sign of clouds, looking for cloud cover in the CTIO RASIMCAM all-sky infrared videos⁴⁶, and, finally, by looking at the scatter in the standard star residuals. The full list of nights for which STDRED was run and the photometric sta-

⁴⁵ <http://www.ctio.noao.edu/noao/node/3176>

⁴⁶ <http://www.ctio.noao.edu/noao/node/2253>

TABLE 6
SMASH MEDIAN PHOTOMETRIC TRANSFORMATION EQUATIONS

Band	Color	Zero-point term	Color term	Extinction term
<i>u</i>	<i>u</i> − <i>g</i>	1.54326 ± 0.0069	0.0142 ± 0.0041	0.3985 ± 0.00240
<i>g</i>	<i>g</i> − <i>r</i>	-0.3348 ± 0.0019	-0.1085 ± 0.0010	0.1747 ± 0.00076
<i>r</i>	<i>g</i> − <i>r</i>	-0.4615 ± 0.0018	-0.0798 ± 0.0011	0.0850 ± 0.00098
<i>i</i>	<i>i</i> − <i>z</i>	-0.3471 ± 0.0016	-0.2967 ± 0.0012	0.0502 ± 0.00058
<i>z</i>	<i>i</i> − <i>z</i>	-0.0483 ± 0.0023	-0.0666 ± 0.0016	0.0641 ± 0.00075

tus are given in `smash_observing_conditions.txt` (in `SMASHRED/obslog/`).

The ~ 3100 variables were not fit to the data simultaneously but were found through an iterative fitting process:

1. Fit all terms separately for all night and chip combinations.
2. Compute the mean color term per chip.
3. Fix color terms and refit zero-point and extinction terms.
4. Average extinction terms. For nights with poor solutions or low airmass ranges a weighted average of the extinction terms of the nearest four neighboring nights is computed. For the rest of the nights, a new extinction term is computed using data included from the four nearest neighboring nights.
5. Fix color and extinction terms and refit zero-point terms.

The final photometric transformation equations are written to file (`smashred_transphot_eqns.fits` available in `SMASHRED/data/`) with zero-point, color and extinction terms (with uncertainties and averaging information) for each night and chip combination, as well as separate tables with information unique to each chip (e.g., color term) and information unique to each night (e.g., extinction term). The formal uncertainties on the terms are: ~ 0.002 , ~ 0.0015 , and ~ 0.0007 for the zero-point, color and extinction, respectively. For an average color and airmass this amounts to a formal uncertainty in the photometry of ~ 0.002 mag (0.009 mag for *u*). Table 6 gives median values and uncertainties per band, while example residuals versus chip, airmass and color for a single night are shown in Figure 7.

The nights of the UT 2014 January 5–7 observing run were clear and photometric but no SDSS standard star observations were taken. Therefore, the regular procedures could not be used to determine the transformation equations for these nights. Subsequently some of the fields from this run could be calibrated because they were reobserved on other photometric nights (with standard star data) or 0.9-m calibration data were obtained. The photometric transformation equations were then determined (“backed-out”) by using these calibrated fields and using the previously derived chip-dependent color terms. The `smashred_transphot_eqns.fits` was then updated with these values and the data for those nights could be calibrated in the regular manner.

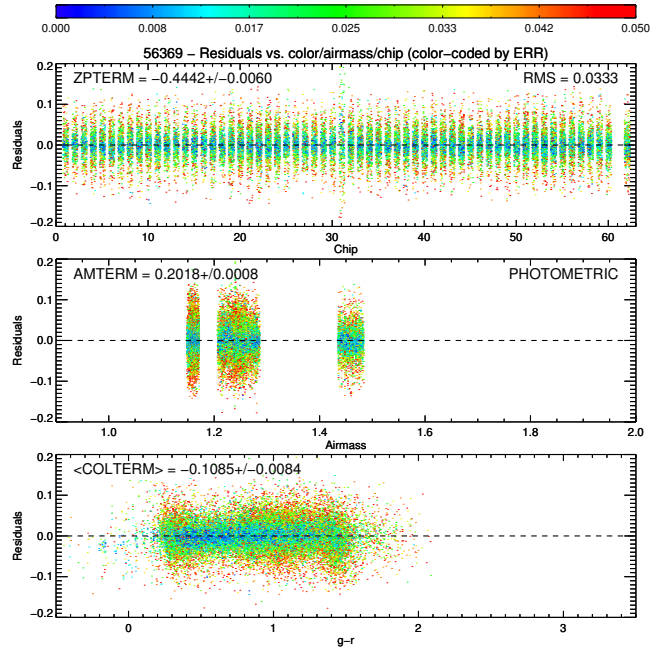


FIG. 7.— The *g*-band residuals (SDSS reference magnitude – derived magnitude using the transformation equations) after fitting the photometric transformation equations to standard star observations for a typical photometric night. The observations are color-coded by their photometric error. (Top) Residuals versus chip number. (Middle) Residuals versus airmass. (Bottom) Residuals versus *g* − *r* color. The derived terms of the photometric transformation equations and their uncertainties are given in the upper left-hand corner of their respective panel.

5.2. Calibration Software

New software was developed to perform calibration of SMASH fields across multiple nights and using a variety of zero-point calibration methods. The software also takes advantage of the overlap of our multiple short exposures with large dithers to tie all of the chip data for a given field onto the same photometric zero-point using an übercal technique. While PHOTRED performs similar tasks (i.e., COMBINE and CALIB), it is on a night-by-night basis. This meant, therefore, that the custom SMASH calibration software needed to start with the instrumental PHOTRED photometry catalogs output by the ASTROM stage.

The calibration follows these steps (in pseudocode):

WHILE calibrated photometry changes >1 mmag:

- The photometry is calibrated using the zero-point (ZPTerm), color (COLTERM) and extinction/airmass terms (AMTerm). This is an

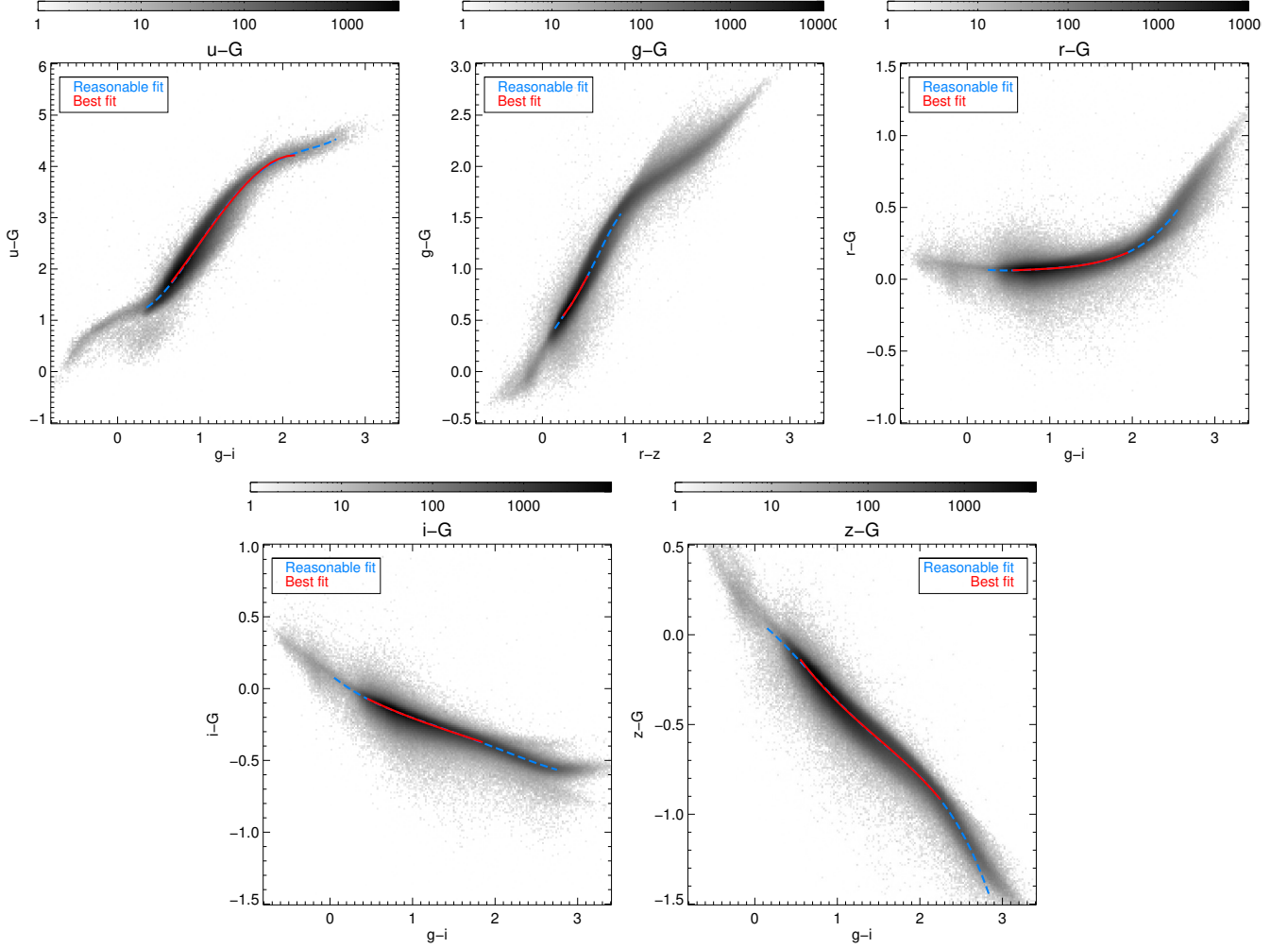


FIG. 8.— SMASH-Gaia color-color distributions and relations. Blue dashed lines are polynomial fits over a “reasonable” color range (avoiding the highest rms regions at the ends) while the solid red lines are polynomial fits over the “best” color range giving the lowest rms scatter. The scatters over the best color ranges are 6% (u), 1% (g), 0.2% (r), 0.4% (i) and 0.5% (z).

iterative process because of the color-term. First, the source photometry is calibrated using the average photometry to construct the color (a color of zero is used on the first iteration), then the photometry is averaged per object and band. The process repeats until all changes are <0.1 mmag. (SMASH_APPLY_PHOTTRANSEQN.PRO)

FOR all filters

1. Measure the pair-wise photometric offsets of overlapping chips (SMASH_MEASURE_MAGOFFSET.PRO).
2. Solve the relative magnitude offsets per chip using the übercal algorithm (SMASH_SOLVE_UBERCAL.PRO).
3. Determine the photometric zero-point (SMASH_SET_ZERPOINTS.PRO).

ENDFOR

ENDWHILE

We employ a simple iterative übercal solving technique (Padmanabhan et al. 2008). After all of the pair-wise photometric offsets of overlapping chips are measured, the robust weighted average offset of a chip relative to its overlapping neighbors is calculated and one half of this is used as the übercal correction for this chip. The pair-wise photometric offsets are updated for these chip-wise corrections and the procedure repeats until convergence is reached (the average relative offset change from one iteration to the next is less than 1%). The changes become very small after only a couple iterations. The cumulative corrections are applied to the chip-wise zero-point terms (ZPTerm) and saved in the UBERCAL_MAGOFFSET columns. The übercal technique only measures and solves for a constant magnitude offset for every chip. There is no allowance for spatial variations across the chip such as due to variable throughput. The outer (while) loop in the calibration is used to make sure the color terms are properly taken into account.

One of three different techniques is employed to set the photometric zero-point of the data depending on the observing conditions and what 0.9-m calibration data are available. The options in decreasing order of preference are:

1. Photometric DECam data (ZPCALIBFLAG=1): Any DECam data taken during photometric conditions (PHOTOMETRIC=1) and having good photometric transformation equations from standard star exposures (BADSOLN=0) are used to set the photometric zero-point. Any non-photometric data are tied to this via the übercal offsets.
2. Overlap with photometric DECam data (ZPCALIBFLAG=2): A field with no photometric data itself but that overlaps a neighboring field (this happens mainly in the central LMC and SMC fields) with photometric data can be calibrated using the overlap. The median offset of bright, high S/N overlap stars is used to set the zero-point.
3. 0.9-m calibration data (ZPCALIBFLAG=3): If a field cannot be calibrated using the first two options and 0.9-m calibration data are available for the field, then it is used to determine the zero-point with the stars detected in both the DECam and 0.9-m data.

For fields where none of these options are available we use SMASH-Gaia color-color relations to calculate rough zero-points. These relations were derived by cross-matching 49 of our SMASH fields with good, calibrated photometry and that lie far from both the LMC and SMC against the Gaia catalog. Bright stars were used to determine the functional relationship between $X_{\text{SMASH}} - G_{\text{Gaia}}$ and a SMASH color ($g-i$ for all SMASH bands except $r-z$ for g). These relations are very tight for the redder bands (r , i , and z) with only a scatter of $\sim 0.5\%$ (see Figure 8), but are poorer and with large color term for the bluer bands (u and g with scatter of $\sim 6\%$ and $\sim 1\%$ respectively).

Once all of the data are calibrated, average coordinates and morphological parameters (e.g., sharp, chi) are computed (weighted averages) from the multiple measurements of each object. We then produce an exposure map for the field in each band (at the pixel level) and use this to sort out non-detections (set to 99.99) from cases of no good data for an object (set to NaN). Schlegel, Finkbeiner & Davis (1998) $E(B-V)$ extinctions are also added for each object, but dereddened magnitudes are not computed. Care should be taken in using the SFD extinction values in the central regions of the MCs because they can be unreliable there and, also, for MW stars for which they can overestimate the foreground dust. Finally, the unique objects are cross-matched with the Gaia, 2MASS and ALLWISE catalogs.

6. DESCRIPTION AND ACHIEVED PERFORMANCE OF FINAL CATALOGS

The SMASH dataset includes 5,809 DECam exposures with 349,046 separate chip files producing 3,992,314,414 independent source measurements of 418,642,941 unique objects (296,223,749 with multiple detections).

6.1. Final Catalog Files

The final catalogs consist of seven gzip-compressed binary FITS files per field:

1. `FIELD_exposures.fits.gz` – Information about each exposure.

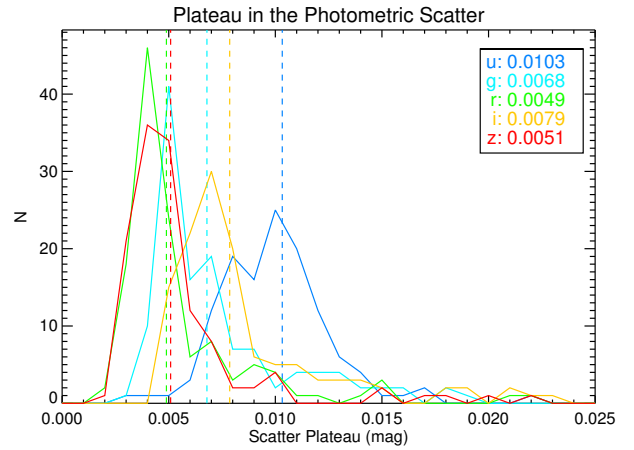


FIG. 9.— The distribution of the lower plateau in the photometric scatter (using multiple measurements of bright stars) in 126 calibrated SMASH fields. This is a good estimate for the photometric precision of the survey. Vertical dashed lines show the median value for each band.

2. `FIELD_chips.fits.gz` – Information about each chip.
3. `FIELD_allsrc.fits.gz` – All of the individual source measurements for this field.
4. `FIELD_allobj.fits.gz` – Average values for each unique object.
5. `FIELD_allobj_bright.fits.gz` – Bright stars from allobj used for cross-matching between fields.
6. `FIELD_allobj_xmatch.fits.gz` – Cross-matches between SMASH and Gaia, 2MASS and ALLWISE.
7. `FIELD_expmap.fits.gz` – The “exposure” map per band.

More detailed descriptions of the catalogs can be found in the PHOTRED “README” file⁴⁷ on the ftp site (see below).

6.2. Photometric Precision

The photometric precision of the final SMASH catalogs can be estimated by calculating the scatter in multiple independent measurements of the same object using bright stars. We measured the minimum of median-binned (0.2 mag bins) photometric scatter values of bright stars for 126 deep and fully-calibrated SMASH fields in each band (see Figure 9). The distributions indicate a precision of roughly 1.0% (u), 0.7% (g), 0.5% (r), 0.8% (i), and 0.5% (z) in the SMASH photometry.

6.3. Photometric Accuracy

To evaluate the accuracy of the photometric calibration, we use the overlap of fields in the LMC/SMC main-body fields that are independently calibrated. Using the scatter in their distributions of mean magnitude offsets (and accounting for the $\sqrt{2}$ because there are contributions from both fields) we obtain rough calibration accuracies of 1.3% (u), 1.3% (g), 1.0% (r), 1.2% (i), and 1.3%

⁴⁷ <ftp://archive.noao.edu/public/hlsp/smash/dr1/photred/README>

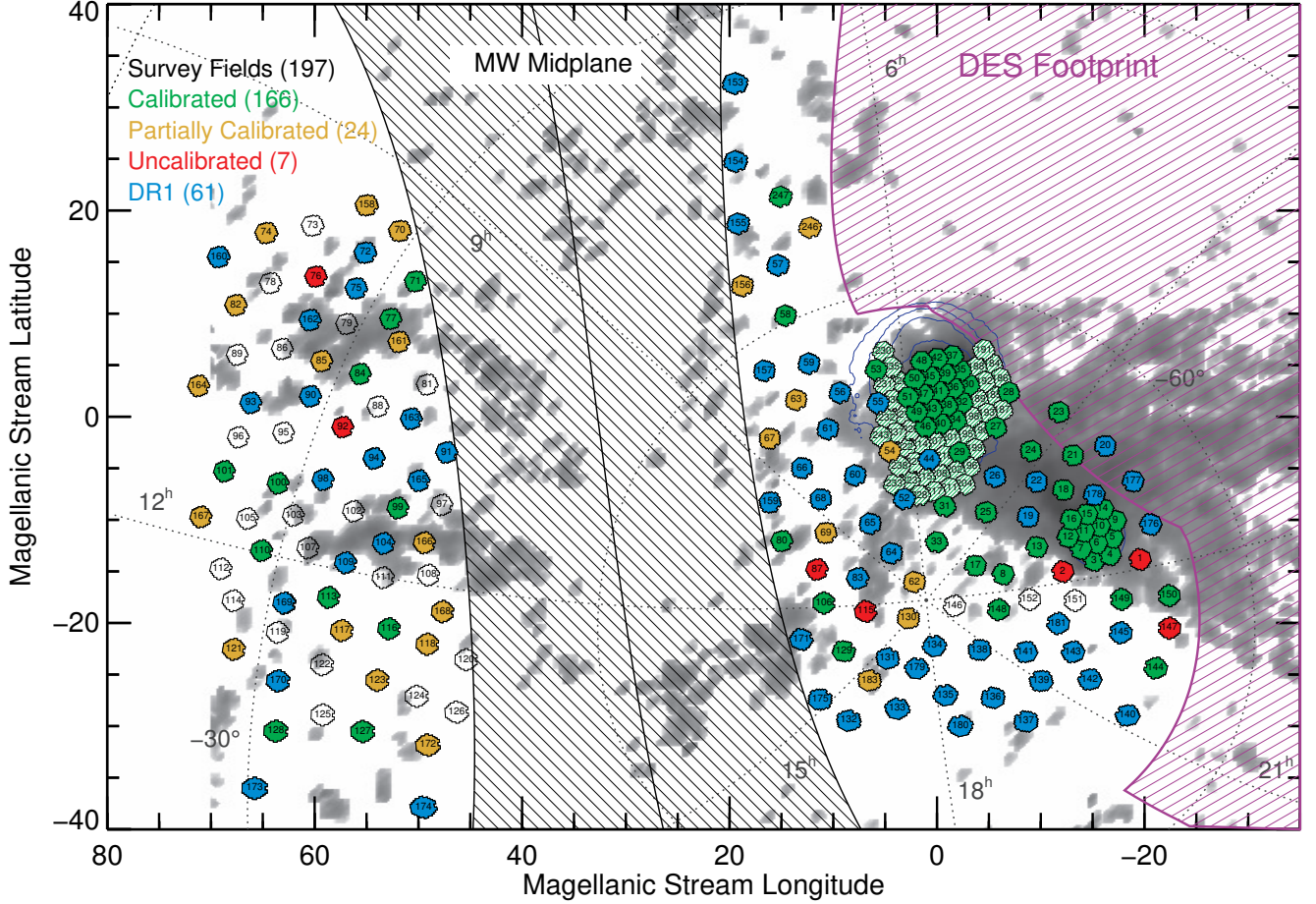


FIG. 10.— The SMASH survey. The observed HI column density of the Magellanic Stream system is shown in grayscale (Nidever et al. 2010). Observed SMASH fields are shown as filled hexagons while unobserved SMASH fields are indicated by open black hexagons. Green (and dark blue) fields are fully calibrated (166 fields), golden are partially calibrated (some bands calibrated and some bands uncalibrated; 24 fields), and red are uncalibrated (7 fields). The green hashed hexagons are the 40 shallow LMC fields. The 61 DR1 fields are shown in dark blue (all fully calibrated). The DES footprint is represented by the purple shaded region.

(z). The low scatter in the SMASH-Gaia color-color relations (especially for the redder bands) also attest to the high quality of the SMASH calibration.

6.4. Photometric Depth

The median 5σ point source depths in $ugriz$ bands are (23.9, 24.8, 24.5, 24.2, 23.5) mag, respectively, which is ~ 2 mags deeper than SDSS and ~ 1.4 mags deeper than Pan-STARRS1.

6.5. Astrometric Performance

The astrometric precision of the individual measurements of bright stars is ~ 20 mas. The precision of the average coordinates of objects (each having ~ 10 – 30 measurements) is ~ 15 mas and is limited by the systematics in the higher-order WCS distortion terms. The astrometric accuracy is ~ 2 mas per coordinate with respect to the Gaia reference frame.

7. FIRST PUBLIC DATA RELEASE

The first SMASH public data release contains ~ 700 million measurements of ~ 100 million objects in 61 deep and fully-calibrated fields sampling the ~ 2400 deg 2 region of the SMASH survey (blue hexagons in Figure 10). The rest of the data will be included in our second

data release in 2018. The main data access is through a prototype version of the NOAO Data Lab⁴⁸. Access and exploration tools include a custom Data Discovery tool, database access to the catalog (via direct query or TAP service), an image cutout service, and a Jupyter notebook server with example notebooks for exploratory analysis. The data release page also gives extensive documentation on the SMASH survey, the observing strategy, data reduction and calibration, as well as information on the individual data products.

Images, intermediate data products, and final catalogs (in FITS binary formats) are also available through the NOAO High Level Data Products FTP site⁴⁹. The raw images as well as the CP-reduced InstCal, Resampled and single-band Stacked images are available in `raw/`, `instcal/`, `resampled/`, and `stacked/` directories, respectively (and grouped in nightly subdirectories). Each subdirectory has a `README` file that gives information about each FITS image file (e.g., exposure number, time stamp, filter, exposure time, field). The PHOTRED-ready FITS files and other associated files (PSF, photometry catalogs, logs, etc.) as well as the multi-band

⁴⁸ <http://datalab.noao.edu/>

⁴⁹ <ftp://archive.noao.edu/public/hlsp/smash/dr1/>

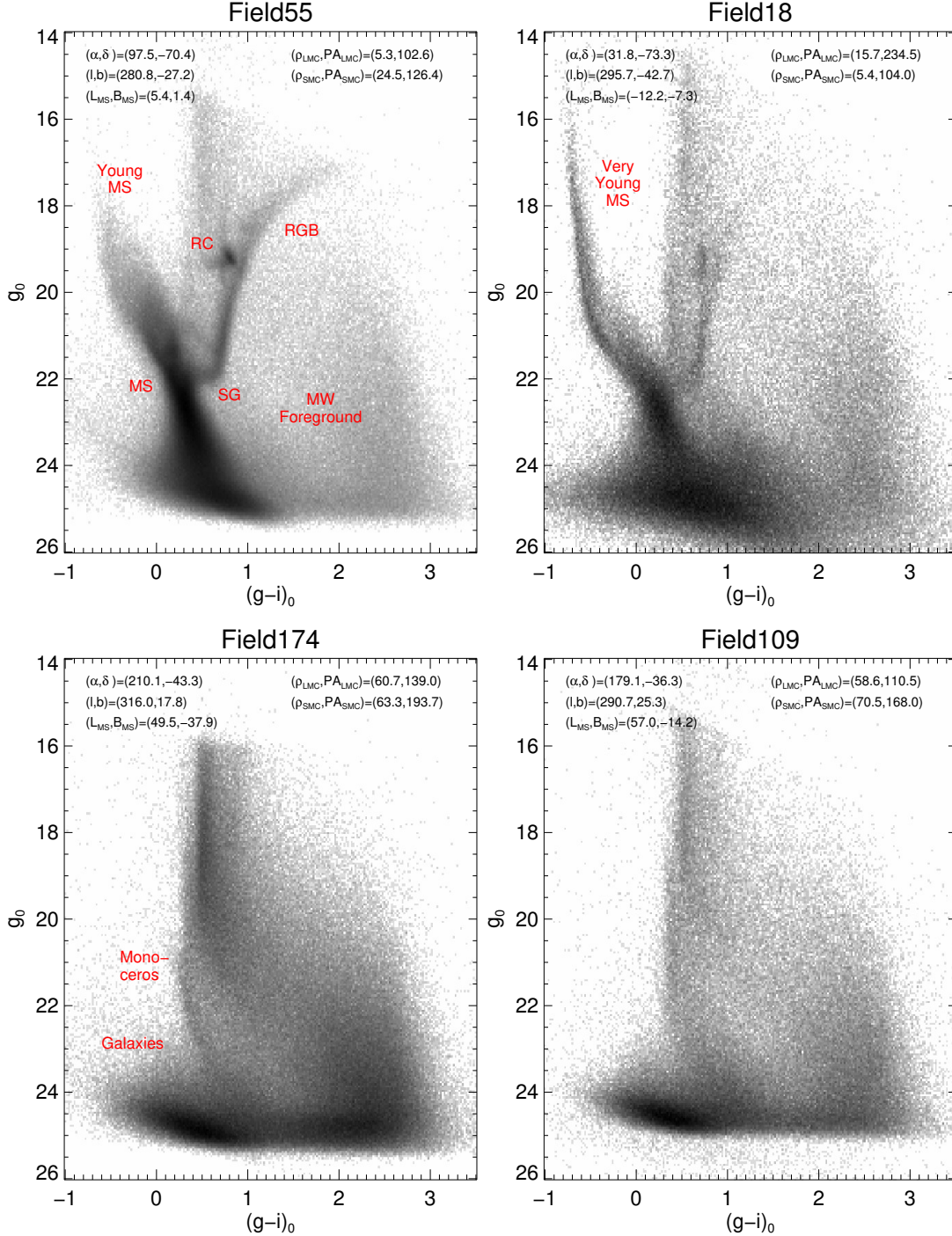


FIG. 11.— Some example SMASH Hess diagrams illustrating the depth and high-quality of the SMASH photometry and diversity of the stellar populations probed. Field55 is on the eastern side of the LMC ($R=5.3^\circ$); Field18 is in the Magellanic Bridge region near the SMC; Field174 is in the Leading Arm region but close to the Milky Way midplane ($b=17.8^\circ$); Field109 is also in the Leading Arm region but at higher Galactic latitude ($b=25.3^\circ$). Equatorial, Galactic and Magellanic Stream coordinates are given in the upper-left corner of each panel, while the radius and position angle with respect to the LMC and SMC are given in the upper-right.

stacks are available in the `photred/` directory. The final binary FITS catalogs (as described in Section 6.1) are in the `catalogs/` directory. Finally, there are seven tables in the database that were populated using the FITS catalogs (but somewhat modified): field, exposure, chip, source, object, and xmatch. The “field” table includes summary information for each field. A detailed description of the database schema (tables and columns) is given

on the SMASH data release website.

8. RESULTS

SMASH is a deep, multi-band photometric survey of the Magellanic Clouds with the goal of mapping the stellar features of these two nearby galaxies to very low surface brightness and thereby providing better understanding of their joint formation and evolution. The data in

the central regions of the Clouds will also be used to obtain spatially-resolved star formation histories of these galaxies to old ages. The data, spanning a region of 2400 deg², have been processed and calibrated to high fidelity with almost four billion measurements of 420 million objects in 197 fields. The data for 61 of these fields and 100 million objects are in the first public data release through the NOAO Data Lab. Figure 11 shows some example Hess diagrams of a number of our SMASH fields, which indicate the depth (~ 2 mag below the oldest main-sequence turnoff in the LMC) and high quality of the SMASH photometry.

The SMASH data have already produced some exciting results. In Martin et al. (2015), we presented the discovery of a compact and faint Milky Way satellite, Hydra II (in Field169), with morphological and stellar population properties consistent with being a dwarf galaxy (also see Kirby et al. 2015). Interestingly, comparison with simulations suggests that, given Hydra II’s position in the sky and distance of ~ 140 kpc (from blue horizontal branch stars), it could be associated with the Leading Arm of the Magellanic Stream. Proper motion information, however, is needed to confirm this possibility. We obtained follow-up time-series data on Hydra II to study its variable stars. This work yielded one RR Lyrae star in Hydra II that gave a slightly larger distance of 151 ± 8 kpc, as well as the discovery of dozens of short period variables in the field (Vivas et al. 2016).

Further sensitive searching for overdensities in the SMASH data yielded the discovery of a compact and very faint ($M_V = -1.0$) stellar system (designated SMASH 1) $\sim 11^\circ$ away from the LMC (Martin et al. 2016). SMASH 1 is consistent with being an old globular cluster in the LMC periphery likely associated with the LMC disk and potentially on the verge of being tidally disrupted.

One of the on-going SMASH projects is to map out the extended stellar populations of the LMC. An analysis of the Hess diagrams indicates that LMC stellar populations can be detected in SMASH data out to 21.1° from the LMC center, or ~ 18.4 kpc, and to surface brightness levels of ~ 33.3 mag arcsec⁻² (D. Nidever et al. 2017, in preparation).

One of the main goals of SMASH is to use the data in the central LMC/SMC fields to derive spatially-resolved star formation histories. The Hess diagram of Field55 in Figure 11 (upper left) is an example of the wealth of information in the data. This field, and other nearby ones show two subgiant branches, which indicates two periods of peak star formation. This was previously only seen in star formation rate diagrams from detailed star formation history modeling (Harris & Zaritsky 2009; Meschin et al. 2014), but now is visually clear just in the Hess diagrams. Full star formation history modeling still awaits computationally intensive artificial star tests for the SMASH data, which will be a focus of on-going SMASH processing efforts in the near future.

The deep and multi-band data in the main bodies of the Magellanic Clouds are also very useful for detecting faint star clusters. We are in the process of developing a citizen science project (led by L.C.J.) based on the SMASH data under the Zooniverse platform⁵⁰ which currently has roughly one million users and hosts many

citizen science projects in multiple scientific disciplines. The project will be called “The Magellanic Project” and will be similar to the “The Andromeda Project” of *HST* images of M31. The citizen scientists will inspect our deep co-add *ugriz* images and visually identify (a) star clusters (open and globular), (b) galaxies behind the LMC/SMC main bodies, (c) and potential new dwarf galaxies of the MW or the MCs. The website is projected to be launched in early 2017.

The SMASH data are also very useful for studying structures in the MW halo that are unrelated to the MCs. The Hess diagram of Field174 in Figure 11 (lower left panel), not far above the MW mid-plane ($b=17.8^\circ$), shows a prominent stellar population at a distance of ~ 10 – 20 kpc (thin sequence with $(g-i)_0 \sim 0.5$ and $21.0 \lesssim g_0 \lesssim 23.5$). Many other fields at low Galactic latitude show similar stellar populations that are very likely associated with the Monoceros “ring” (e.g., Slater et al. 2014). There are on-going SMASH projects to study these and similar MW halo structures in the SMASH data.

The SMASH survey has the potential to revolutionize our understanding of the stellar populations inside and in the very outskirts of two canonical examples of dwarf galaxies, the SMC and LMC.

DLN was supported by a McLaughlin Fellowship while at the University of Michigan. YC acknowledges support from NSF grant AST 1655677. EFB acknowledges support from NSF grants AST 1008342 and 1655677. EWO was partially supported by NSF grant AST 1313006. TdB acknowledges financial support from the ERC under Grant Agreement n. 308024. M-RC acknowledges support by the German Academic Exchange Service (DAAD), from the UK’s Science and Technology Facility Council [grant number ST/M001008/1], and from the the European Research Council (ERC) under the European Union’s Horizon 2020 research and innovation programme (grant agreement No 682115). SJ is supported by the Netherlands Organization for Scientific Research (NWO) Veni grant 639.041.131. SRM acknowledges partial support from NSF grant AST 1312863. DM-D acknowledges support by Sonderforschungsbereich (SFB) 881 “The Milky Way System” of the German Research Foundation (DFB), subproject A2. RRM acknowledges partial support from CONICYT Anillo project ACT-1122 and project BASAL PFB-06. GSS is supported by grants from NASA. Based on observations at Cerro Tololo Inter-American Observatory, National Optical Astronomy Observatory (NOAO Prop. ID: 2013A-0411 and 2013B-0440; PI: Nidever), which is operated by the Association of Universities for Research in Astronomy (AURA) under a cooperative agreement with the National Science Foundation. IRAF is distributed by the National Optical Astronomy Observatory, which is operated by the Association of Universities for Research in Astronomy (AURA) under a cooperative agreement with the National Science Foundation. This project used data obtained with the Dark Energy Camera (DECam), which was constructed by the Dark Energy Survey (DES) collaboration. Funding for the DES Projects has been provided by the U.S. Department of Energy, the U.S. National Science Foundation, the Ministry of Science and

⁵⁰ <https://www.zooniverse.org>

Education of Spain, the Science and Technology Facilities Council of the United Kingdom, the Higher Education Funding Council for England, the National Center for Supercomputing Applications at the University of Illinois at Urbana-Champaign, the Kavli Institute of Cosmological Physics at the University of Chicago, Center for Cosmology and Astro-Particle Physics at the Ohio State University, the Mitchell Institute for Fundamental Physics and Astronomy at Texas A&M University, Financiadora de Estudos e Projetos, Fundação Carlos Chagas Filho de Amparo, Financiadora de Estudos e Projetos, Fundação Carlos Chagas Filho de Amparo à Pesquisa do Estado do Rio de Janeiro, Conselho Nacional de Desenvolvimento Científico e Tecnológico and the Ministério da Ciência, Tecnologia e Inovação, the Deutsche Forschungsgemeinschaft and the Collaborating Institutions in the Dark Energy Survey. The Collaborating Institutions are Argonne National Laboratory, the

University of California at Santa Cruz, the University of Cambridge, Centro de Investigaciones Energéticas, Medioambientales y Tecnológicas-Madrid, the University of Chicago, University College London, the DES-Brazil Consortium, the University of Edinburgh, the Eidgenössische Technische Hochschule (ETH) Zürich, Fermi National Accelerator Laboratory, the University of Illinois at Urbana-Champaign, the Institut de Ciències de l'Espai (IEEC/CSIC), the Institut de Física d'Altes Energies, Lawrence Berkeley National Laboratory, the Ludwig-Maximilians Universität München and the associated Excellence Cluster Universe, the University of Michigan, the National Optical Astronomy Observatory, the University of Nottingham, the Ohio State University, the University of Pennsylvania, the University of Portsmouth, SLAC National Accelerator Laboratory, Stanford University, the University of Sussex, and Texas A&M University.

REFERENCES

- Dark Energy Survey Collaboration, Abbott, T., Abdalla, F. B., et al. 2016, *MNRAS*, 460, 1270
- Alam, S., Albareti, F. D., Allende Prieto, C., et al. 2015, *ApJS*, 219, 12
- Bechtol, K., Drlica-Wagner, A., Balbinot, E., et al. 2015, *ApJ*, 807, 50
- Belokurov, V., Irwin, M. J., Koposov, S. E., Evans, N. W., Gonzalez-Solares, E., Metcalfe, N., & Shanks, T. 2014, *MNRAS*, 441, 2124
- Belokurov, V., & Koposov, S. E. 2016, *MNRAS*, 456, 602
- Belokurov, V., Erkal, D., Deason, A. J., et al. 2016, *arXiv:1611.04614*
- Bertin, E., & Arnouts, S. 1996, *A&AS*, 117, 393
- Besla, G., Kallivayalil, N., Hernquist, L., Robertson, B., Cox, T. J., van der Marel, R. P., & Alcock, C. 2007, *ApJ*, 668, 949
- Besla, G., Kallivayalil, N., Hernquist, L., van der Marel, R. P., Cox, T. J., & Kereš, D. 2010, *ApJ*, 721, L97
- . 2012, *MNRAS*, 421, 2109
- Besla, G., Hernquist, L., & Loeb, A. 2013, *MNRAS*, 428, 2342
- Besla, G., Martínez-Delgado, D., van der Marel, R. P., et al. 2016, *ApJ*, 825, 20
- Brüns, C., et al. 2005, *A&A*, 432, 45B
- Chambers, K. C., Magnier, E. A., Metcalfe, N., et al. 2016, *arXiv:1612.05560*
- Connors, T. W., Kawata, D., Maddison, S. T., & Gibson, B. K. 2004, *PASA*, 21, 222
- Connors, T. W., Kawata, D., & Gibson, B. K. 2006, *MNRAS*, 371, 108
- Drlica-Wagner, A., Bechtol, K., Rykoff, E. S., et al. 2015, *ApJ*, 813, 109
- Drlica-Wagner, A., Bechtol, K., Allam, S., et al. 2016, *ApJ*, 833, L5
- Gaia Collaboration, Brown, A. G. A., Vallenari, A., et al. 2016, *A&A*, 595, A2
- Chabrier, G. 2001, *ApJ*, 554, 1274
- Cioni, M.-R. L. 2009, *A&A*, 506, 1137
- Deason, A. J., Belokurov, V., & Evans, N. W. 2011, *MNRAS*, 416, 2903
- Deason, A. J., Belokurov, V., & Weisz, D. R. 2015, *MNRAS*, 448, L77
- Deason, A. J., Wetzel, A. R., Garrison-Kimmel, S., & Belokurov, V. 2015, *MNRAS*, 453, 3568
- De Propriis, R., Rich, R. M., Mallery, R. C., & Howard, C. D. 2010, *ApJ*, 714, L249
- de Vaucouleurs, G. 1955, *AJ*, 60, 219
- D'Onghia, E., & Lake, G. 2008, *ApJ*, 686, L61
- Diaz, J. D., & Bekki, K. 2012, *ApJ*, 750, 36
- Epchtein, N., de Batz, B., Capolani, L., et al. 1997, *The Messenger*, 87, 27
- Fox, A. J., Wakker, B. P., Smoker, J. V., et al. 2010, *ApJ*, 718, 1046
- Flaugher, B., Diehl, H. T., Honscheid, K., et al. 2015, *AJ*, 150, 150
- Gallart, C., Stetson, P. B., Meschin, I. P., Pont, F., & Hardy, E. 2008, *ApJ*, 682, L89
- Gardiner, L. T., & Hawkins, M. R. S. 1991, *MNRAS*, 251, 174
- Gardiner, L. T., & Hatzidimitriou, D. 1992, *MNRAS*, 257, 195
- Gardiner, L. T. & Noguchi, M. 1996, *MNRAS*, 278, 191
- Harris, J., & Zaritsky, D. 2006, *AJ*, 131, 2514
- Harris, J., & Zaritsky, D. 2009, *AJ*, 138, 1243
- Hatzidimitriou, D., Hawkins, M. R. S., & Gyldenkerne, K. 1989, *MNRAS*, 241, 645
- Hatzidimitriou, D., & Hawkins, M. R. S. 1989, *MNRAS*, 241, 667
- Ivezić, Ž., Sesar, B., Jurić, M., et al. 2008, *ApJ*, 684, 287-325
- Jethwa, P., Erkal, D., & Belokurov, V. 2016, *MNRAS*, 461, 2212
- Kaiser, N., Burgett, W., Chambers, K., et al. 2010, *Proc. SPIE*, 7733, 77330E
- Kallivayalil, N., van der Marel, R. P., Alcock, C., Axelrod, T., Cook, K. H., Drake, A. J., & Geha, M. 2006a, *ApJ*, 638, 772
- Kallivayalil, N., van der Marel, R. P., & Alcock, C. 2006b, *ApJ*, 652, 1213
- Kallivayalil, N., van der Marel, R. P., Besla, G., Anderson, J., & Alcock, C. 2013, *ApJ*, 764, 161
- Kirby, E. N., Simon, J. D., & Cohen, J. G. 2015, *ApJ*, 810, 56
- Koposov, S. E., Belokurov, V., Torrealba, G., & Evans, N. W. 2015, *ApJ*, 805, 130
- Kunkel, W. E., Irwin, M. J., & Demers, S. 1997, *A&AS*, 122, 1
- Kunkel, W. E., Demers, S., & Irwin, M. J. 2000, *AJ*, 119, 2789
- Lynden-Bell, D. 1976, *MNRAS*, 174, 695
- Mackey, A. D., Koposov, S. E., Erkal, D., et al. 2016, *MNRAS*, 459, 239
- Majewski, S. R., Nidever, D. L., Muñoz, R. R., et al. 2009, *The Magellanic System: Stars, Gas, and Galaxies*, 256, 51
- Martin, N. F., Nidever, D. L., Besla, G., et al. 2015, *ApJ*, 804, L5
- Martin, N. F., Jungbluth, V., Nidever, D. L., et al. 2016, *ApJ*, 830, L10
- Mastropietro, C., Moore, B., Mayer, L., Wadsley, J., & Stadel, J. 2005, *MNRAS*, 363, 509
- Mateo, M. L. 1998, *ARA&A*, 36, 435
- McConnachie, A. W. 2012, *AJ*, 144, 4
- Meschin, I., Gallart, C., Aparicio, A., Hidalgo, S. L., Monelli, M., Stetson, P. B., & Carrera, R. 2014, *MNRAS*, 438, 1067
- Minniti, D., Borissova, J., Rejkuba, M., Alves, D. R., Cook, K. H., & Freeman, K. C. 2003, *Science*, 301, 1508
- Monet, D. G., Levine, S. E., Canzian, B., et al. 2003, *AJ*, 125, 984
- Miknaitis, G., et al. 2007, *ApJ*, 666, 674
- Muller, E., Staveley-Smith, L., Zealey, W., & Stanimirović, S. 2003, *MNRAS*, 339, 105
- Muñoz, R. R., Majewski, S. R., Zaggia, S., et al. 2006, *ApJ*, 649, 201
- Murai, T., & Fujimoto, M. 1980, *PASJ*, 32, 581
- Nidever, D. L., Majewski, S. R., & Burton, W. B. 2008, *ApJ*, 679, 432
- Nidever, D. L., Majewski, S. R., Burton, W. B., & Nigra, L. 2010, *ApJ*, 723, 1618

- Nidever, D. L., Majewski, S. R., Muñoz, R. R., Beaton, R. L., Patterson, R. J., & Kunkel, W. E. 2011, *ApJ*, 733, L10
- Nidever, D. L., Monachesi, A., Bell, E. F., Majewski, S. R., Muñoz, R. R., & Beaton, R. L. 2013, *ApJ*, 779, 145
- Noël, N. E. D., & Gallart, C. 2007, *ApJ*, 665, L23
- Noël, N. E. D., Gallart, C., Costa, E., & Méndez, R. A. 2007, *AJ*, 133, 2037
- Noël, N. E. D., Aparicio, A., Gallart, C., Hidalgo, S. L., Costa, E., Noël, N. E. D., Conn, B. C., Carrera, R., Read, J. I., Rix, H.-W., & Dolphin, A. 2013, *ApJ*, 768, 109
- Olano, C. A. 2004, *A&A*, 423, 895
- Olsen, K. A. G., Zaritsky, D., Blum, R. D., Boyer, M. L., & Gordon, K. D. 2011, *ApJ*, 737, 29
- Padmanabhan, N., et al. 2008, *ApJ*, 674, 1217
- Pierres, A., Santiago, B. X., Drlica-Wagner, A., et al. 2016, *arXiv:1612.03938*
- Putman, M. E., Staveley-Smith, L., Freeman, K. C., Gibson, B. K., & Barnes, D. G. 2003, *ApJ*, 586, 170 (P03)
- Rest, A., et al. 2005, *ApJ*, 634, 1103
- Saha, A., Olszewski, E. W., Brondel, B., et al. 2010, *AJ*, 140, 1719
- Sales, L. V., Navarro, J. F., Cooper, A. P., White, S. D. M., Frenk, C. S., & Helmi, A. 2011, *MNRAS*, 418, 648
- Sales, L. V., Navarro, J. F., Kallivayalil, N., & Frenk, C. S. 2017, *MNRAS*, 465, 1879
- Schlafly, E. F., & Finkbeiner, D. P. 2011, *ApJ*, 737, 103
- Schlegel, D. J., Finkbeiner, D. P., & Davis, M. 1998, *ApJ*, 500, 525
- Skrutskie, M. F., Cutri, R. M., Stiening, R., et al. 2006, *AJ*, 131, 1163
- Stanimirović, S., Staveley-Smith, L., Dickey, J. M., Sault, R. J., & Snowden, S. L. 1999, *MNRAS*, 302, 417
- Stanimirović, S., Dickey, J. M., Krčo, M., & Brooks, A. M. 2002, *ApJ*, 576, 773
- Stanimirović, S., Staveley-Smith, L., & Jones, P. A. 2004, *ApJ*, 604, 176
- Staveley-Smith, L., Kim, S., Calabretta, M. R., Haynes, R. F., & Kesteven, M. J. 2003, *MNRAS*, 339, 87 (S03)
- Slater, C., Bell, E. F., Schlafly, E. F., et al. 2014, *ApJ*, 791, 9
- Smith, J. A., Tucker, D. L., Kent, S., et al. 2002, *AJ*, 123, 2121
- Stetson, P. B. 1987, *PASP*, 99, 191
- Stetson, P. B. 1990, *PASP*, 102, 932
- . 1994, *PASP*, 106, 250
- van der Marel, R. P., & Cioni, M.-R. L. 2001, *AJ*, 122, 1807
- van der Marel, R. P. 2001, *AJ*, 122, 1827
- van der Marel, R. P., Alves, D. R., Hardy, E., & Suntzeff, N. B. 2002, *AJ*, 124, 2639
- Valdes, F., Gruendl, R., & DES Project 2014, *Astronomical Data Analysis Software and Systems XXIII*, 485, 379
- Vivas, A. K., Olsen, K., Blum, R., et al. 2016, *AJ*, 151, 118
- Walker, M. G., Mateo, M., Olszewski, E. W., et al. 2016, *ApJ*, 819, 53
- Yoshizawa, A. M., & Noguchi, M. 2003, *MNRAS*, 339, 1135
- York, D. G., Adelman, J., Anderson, J. E., Jr., et al. 2000, *AJ*, 120, 1579
- Zacharias, N., Finch, C. T., Girard, T. M., et al. 2013, *AJ*, 145, 44
- Zaritsky, D., Harris, J., Thompson, I. B., Grebel, E. K., & Massey, P. 2002, *AJ*, 123, 855